Boron nitride nanotube-modified silicon oxycarbide ceramic composite: synthesis, characterization and applications in electrochemical energy storage

by

MONSURU A. ABASS

B.Tech., Federal University of Technology, Akure, Nigeria, 2012
MSc., University of Exeter, United Kingdom, 2015

A THESIS

submitted in partial fulfillment of the requirements for the degree

MASTER OF SCIENCE

Department of Mechanical and Nuclear Engineering
College of Engineering

KANSAS STATE UNIVERSITY
Manhattan, Kansas

2017

Approved by:

Major Professor
Dr. Gurpreet Singh

Copyright

MONSURU A. ABASS

2017

Abstract

Polymer-derived ceramics (PDCs) such as silicon oxycarbide (SiOC) have shown promise as an electrode material for rechargeable Li-ion batteries (LIBs) owing to the synergy between its disordered carbon phase and hybrid bonds of silicon with oxygen and carbon. In addition to their unique structure, PDCs are known for their high surface area (~822.7 m^2 g^{-1}), which makes them potential candidates for supercapacitor applications. However, low electrical conductivity, voltage hysteresis, and first cycle lithium irreversibility have hindered their introduction into commercial devices. One approach to improving charge storage capacity is by interfacing the preceramic polymer with boron or aluminium prior pyrolysis. Recent research has shown that chemical interfacing with elemental boron, bulk boron powders and even exfoliated sheets of boron nitride leads to enhancements in thermal and electronic properties of the ceramic.

This thesis reports the synthesis of a new type of PDC composite comprising of SiOC embedded with boron nitride nanotubes (BNNTs). This was achieved through the introduction of BNNT in SiOC pre-ceramic polymer at varying wt.% loading (0.25, 0.5 and 2.0 wt.%) followed by thermolysis at high temperature. Electron microscopy and a range of spectroscopy techniques were employed to confirm the polymer-to-ceramic transformation and presence of disordered carbon phase. Transmission electron microscopy confirmed the tubular morphology of BNNT in the composite. To test the material for electrochemical applications, the powders were then made into free-standing paper-like electrodes with reduced graphene oxide (rGO) acting as support material.

The synthesized free-standing electrodes were characterized and tested as electrochemical energy storage materials for LIBs and symmetric supercapacitor applications. Among the SiOC-

BNNT composite paper tested as anode materials for LIBs, the 0.25 wt.% BNNT composite paper demonstrated the highest first cycle lithiation capacity corresponding to 812 mAh g^{-1} (at a current density of 100 mA g^{-1}) with a stable charge capacity of 238 mAh g^{-1} when asymmetrically cycled after 25 cycles. On the contrary, the 0.5 wt.% BNNT composite paper demonstrated the highest specific capacitance corresponding to 78.93 F g^{-1} at a current density of 1 A g^{-1} and a cyclic retention of 86% after 185 cycles. This study shows that the free carbon content of SiOC-BNNT ceramic composite can be rationally modified by varying the wt.% of BNNT. As such, the paper composite can be used as an electrode material for electrochemical energy storage.

1

Table of Contents

List of Figures

List of Tables

Acknowledgements

I owe a debt of gratitude to my research and academic advisor, Dr. Gurpreet Singh for refining my work ethics and providing me valuable insights that are required to survive in today's challenging world. I would also like to express my gratitude to my committee members, Dr. Amy Betz and Prof. Keith Hohn for proofreading my thesis and providing suggestions.

Special thanks to Prof. William Dunn, Department Head of Mechanical and Nuclear Engineering (MNE) for approving my department travel grant to support my research. Prof. Steven Eckels deserves a recognition for offering me his words of wisdom and encouragement. Thank you, Dr. Daniel Boyle, for working me into the world of Spectroscopy. Thank you, Dr. Christel Gervais, (Chimie de la Matière Condensée de Paris, France) for helping me with ^{11}B MAS NMR spectroscopy and contribution to my scholarly work. Thank you to Mr. Gary Zito for providing access to the transmission electron microscope facility at Colorado School of Mines.

I would like to thank Prof. Saugata Datta, Ian Andree and Michael Heidlage for training me on XRD without a requesting a dime. Much appreciation goes out to the faculty and staff of the Department of MNE, Phi Kappa Phi, the National Society of Black Engineers, the KSU Graduate Student Council and my lab group members for their support during my studies at KSU.

To my family, especially my humble mom, you are the reason I never gave up. My 'Kansas story' is not complete without the lifelong friendship I have forged with the caring people of Manhattan, Kansas, my roommates and most importantly the Muslim community for nourishing my faith.

Dedication

This thesis is dedicated to those who believed and invested in my dreams; most importantly, my mum.

If I have seen further, it is by standing on the shoulders of giants

… Isaac Newton

Chapter 1 Introduction

1.1 Motivation

Ever since their discovery, fossil fuel has been the major energy source of the world.[1] Their high volumetric energy density (as evidenced in Figure 1-1)[2] coupled with the ease of exploring them from the earth crust have made them an indispensable source of energy. With the exponential increase in the global consumption of fossil fuels resulting in the dwindling price of petroleum in the global energy market, emission of greenhouse gases (a major culprit of global warming), destruction of ecology and depletion of natural reserves of fossil fuel, the search for sustainable and commercially viable alternative energy source popularly known as *renewable energy* have become imperative.
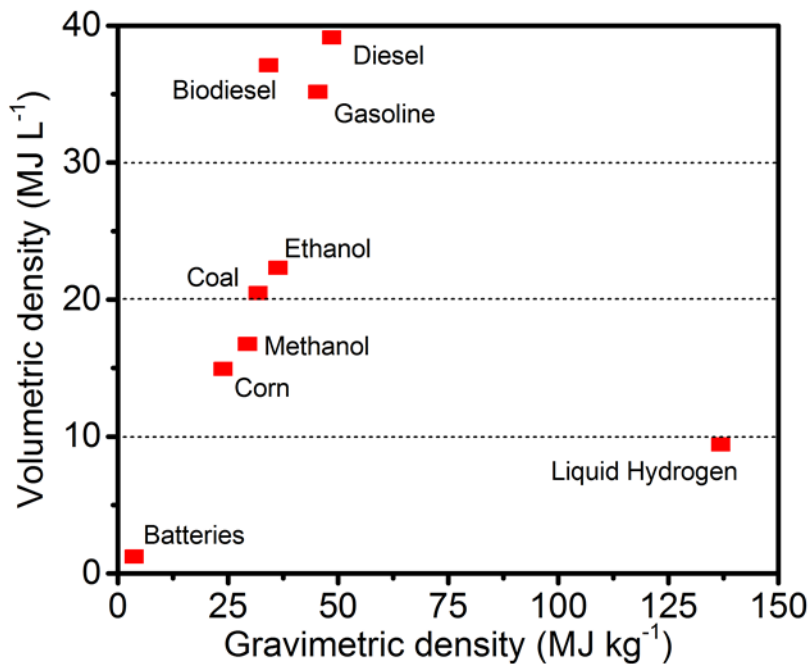
Figure 1-1 Comparative energy density of some fossil fuels with other energy source (Adapted from ref.[2]).

Over the past five years, the world has experienced an influx of renewable energy technology with solar and wind energy technology dominating the renewable energy market.[3] However, the supply of these renewable energy sources is subject to weather condition and location, which cannot be relied upon. In order to realize the potential of emerging technologies such as hybrid electric vehicles, computers, mobile phones etc., portable off-grid power supplies will play a critical role.[4] Such energy system would be required to store energy either from renewable or non-renewable sources and also to combine desirable properties of renewable and non-renewable energy which includes higher energy and power density, longer life cycle, eco-friendliness, high safety level, light weight at very low cost.[5] One class of energy storage technologies that have shown promise for satisfying the aforementioned properties is electrical energy storage (EES) device based on electrochemical processes such as batteries, supercapacitors and recently fuel cells.[6]

Among these EES technologies, rechargeable batteries (mostly lithium-ion batteries (LIBs)) have dominated the global energy market owing to their high energy density, high working voltage, cyclic performance, low self-discharge and relatively high thermal stability. These properties make LIBs a standard power source for portable electronics and recently, automotive systems. However, full realization of LIBs potential is limited by their inadequate energy and power density (compared to the internal combustion engine), slow charging, short life span, safety concerns, battery shape and mechanical properties.[7,8]

Traditional materials for commercial LIBs comprises of a graphite anode on a copper substrate, a lithium intercalated compound cathode such as lithium cobalt oxide ($LiCoO_2$) on an aluminium substrate and a liquid electrolyte.[9] Because charge storage occurs in the anode of LIBs, considerable research have been geared towards improving the capacity of anode materials. As

such, graphite has been used as anode materials for LIBs owing to its good rate performance, high abundance on earth and low cost.[10] However, its capacity is not competitive enough to meet the requirement of today's portable energy demand partly due to its limited theoretical capacity (ca. 370 mAh g^{-1}).[4] For this reason, some class of materials such as graphene-related materials have been touted to show promise for enhancing the performance and cyclability of LIBs either when used as stand-alone materials or incorporated with other materials to form functional nanocomposites.[11–13]

In spite of the strident advances made in the field of energy storage technology using the underlying principles of nanotechnology, no single EES is capable of satisfying the high demands of today's energy needs at reduced cost.[5] A viable solution is to combine various EES technologies. One emerging EES device that could be coupled with LIBs are supercapacitors.[8] Such hybrid EES technology would make up for the low power density of batteries since supercapacitors are known for their high power density and cyclic stability. The realisation of this feat will be anchored on functional materials that are capable of combining the chemistries of batteries and supercapacitors.

In this context, the electrochemical properties of a novel class of organosilicon-based ceramic composites known as polymer-derived ceramics (PDCs) have shown significant promise as an electrochemical energy storage material and have attracted substantial application.[14] This material combines the desirable property of disordered carbon coordinated to silicon (Si) and other functional groups. When integrated with reduced graphene oxide (rGO), PDCs can be made into electroactive electrodes with tremendously improved reversible capacity due to the synergistic effects between both materials.[4,11,12,15–17] In addition, such composite would obviate the need for metal support, binders and conducting agent whilst reducing the overall weight of the electrode material.[11,12,17]

In an attempt to understand the influence of interfacing PDCs with boron nitride nanotube (BNNT) - a ceramic nanomaterial known for its remarkable thermal conductivity, chemical and thermal stability,[18] - this thesis describes electrochemical performance of a LIB anode and symmetric supercapacitor fabricated from a type of PDC material known as silicon oxycarbide (SiOC) modified with BNNTs and supported on rGO.

1.2 Aims and Objectives of Thesis

The aims of this thesis are as follows:

- Synthesis of a lightweight BNNT-modified SiOC ceramic (SiOC-BNNT) supported on rGO

- Evaluation of electrochemical performance of the synthesized ceramic composite as an electrode material for LIB anode material and supercapacitor

The objectives of this thesis are summarized as follows:

- Polymer-to-ceramic conversion of BNNT-modified polymeric precursor of SiOC via controlled pyrolysis in argon environment

- Conversion of SiOC-BNNT ceramic into composite via dispersion in graphene oxide (GO) liquid suspension and subsequent fabrication into paper electrode via vacuum filtration

- Controlled annealing of fabricated paper electrode in order to reduce GO present in the paper to rGO and also stabilize the paper

- Characterization of the synthesized electrode material using relevant characterization techniques

1.3 Overview of Thesis

Chapter 1 introduces the general motivation for this study and also highlights the aims and objectives of the thesis.

Chapter 2 describes the theoretical background of LIBs and supercapacitors, introduces PDCs and provides a review on the electrochemical properties of SiOC as LIB anodes and supercapacitors.

Chapter 3 presents the materials and method used to fabricate thin-film SiOC-BNNT ceramic composite supported on rGO, techniques used to characterize the synthesized ceramic, fabricate the electrode and study the electrochemical performance of the composite as LIB anode and supercapacitor electrode.

Chapter 4 presents the results and analyses of the data and discusses the electrochemical performance of the tested SiOC-BNNT ceramic composites as a LIB anode and supercapacitor.

Chapter 5 concludes the thesis and proposes some recommendations for improving the electrochemical performance of the synthesized SiOC-BNNT ceramic composites as electrode materials for LIB and supercapacitor.

1.4 References

1.   Rusman, N. A. A. & Dahari, M. A review on the current progress of metal hydrides material for solid-state hydrogen storage applications. *Int. J. Hydrogen Energy* **41,** 12108–12126 (2016).

2.   Fischer, M., Werber, M. & Schwartz, P. V. Batteries: Higher energy density than gasoline? *Energy Policy* **37,** 2639–2641 (2009).

3.   U.S Energy Information Administration. Solar, natural gas, wind make up most 2016 generation additions - Today in Energy - U.S. Energy Information Administration (EIA). *Electric Power Monthly* (2016). at <https://www.eia.gov/todayinenergy/detail.php?id=25172>

4.   Fukui, H. *et al.* Lithiation and delithiation of silicon oxycarbide single particles with a unique microstructure. *ACS Appl. Mater. Interfaces* **3,** 2318–2322 (2011).

5.   Chen, G. Z. Understanding supercapacitors based on nano-hybrid materials with interfacial conjugation. *Prog. Nat. Sci. Mater. Int.* **23,** 245–255 (2013).

6.   Winter, M. & Brodd, R. J. What are batteries, fuel cells, and supercapacitors? *Chem. Rev.* **104,** 4245–4269 (2004).

7.   Hu, H. *et al.* Non-covalent functionalization of graphene with bisphenol a for high-performance supercapacitors. *Chinese J. Chem.* **33,** 199–206 (2015).

8.   Zhang, S. & Pan, N. Supercapacitors Performance Evaluation. *Adv. Energy Mater.* **5,** 1401401 (2015).

9.   Bruce, P. G., Freunberger, S. A., Hardwick, L. J. & Tarascon, J.-M. Li–O2 and Li–S batteries with high energy storage. *Nat. Mater.* **11,** 19–29 (2011).

10.   Zhang, W. J. A review of the electrochemical performance of alloy anodes for lithium-ion batteries. *J. Power Sources* **196,** 13–24 (2011).

11.   David, L., Shareef, K. M., Abass, M. A. & Singh, G. Three-dimensional polymer-derived ceramic/graphene paper as a Li-ion battery and supercapacitor electrode. *RSC Adv.* **6,**

53894–53902 (2016).

12.   Kolathodi, M. S., David, L., Abass, M. A. & Singh, G. Polysiloxane-functionalized graphene oxide paper: pyrolysis and performance as a Li-ion battery and supercapacitor electrode. *RSC Adv.* **6,** 74323–74331 (2016).

13.   Sun, H. *et al.* Binder-free graphene as an advanced anode for lithium batteries. *J. Mater. Chem. A* **4,** 6886–6895 (2016).

14.   Colombo, P., Mera, G., Riedel, R. & Sorarù, G. D. Polymer-Derived Ceramics: 40 Years of Research and Innovation in Advanced Ceramics. *J. Am. Ceram. Soc.* **93,** no-no (2010).

15.   Bhandavat, R. & Singh, G. Stable and efficient li-ion battery anodes prepared from polymer-derived silicon oxycarbide-carbon nanotube shell/core composites. *J. Phys. Chem. C* **117,** 11899–11905 (2013).

16.   Shen, J. & Raj, R. Silicon-oxycarbide based thin film anodes for lithium ion batteries. *J. Power Sources* **196,** 5945–5950 (2011).

17.   David, L., Bhandavat, R., Barrera, U. & Singh, G. Silicon oxycarbide glass-graphene composite paper electrode for long-cycle lithium-ion batteries. *Nat. Commun.* **7,** 10998 (2016).

18.   Weng, Q., Wang, X., Wang, X., Bando, Y. & Golberg, D. Functionalized hexagonal boron nitride nanomaterials: emerging properties and applications. *Chem. Soc. Rev.* **45,** 3989–4012 (2016).

Chapter 2 Background of Energy Storage in Lithium-ion Batteries and Supercapacitors

2.1 Lithium-ion Battery

A battery is a device that consist of one or more electrochemical cells that stores and convert electrical energy into chemical energy and vice versa via reduction and oxidation (redox) reactions.[1] Each cell of a battery is composed of two electron-conducting material (known as *electrodes*) in contact with an ionically conducting but electronically insulating medium known as the *electrolyte*. The electrolyte causes the electron to flow into the external circuit where work is done.[2] The electrodes are of two types namely: *anode* and *cathode* – which are ideally made to have a high surface area to ease ionic mobility of the conducting species back and forth.[2] When a battery is connected to an external circuit for power supply, metal ions in the electrolyte are shuttled from the anode to the cathode. This process is accompanied by the simultaneous release of an equivalent number of electrons into the external circuit from the anode. A battery is termed *rechargeable* or *secondary battery* if it can reversibly store metal ions at its electrodes. Otherwise, such battery is termed *non-rechargeable* or *primary battery*.[2]

Lithium-ion batteries (LIBs) belong to the class of rechargeable batteries. They are called *lithium-ion batteries* because their ionic charge carrier is lithium ion (Li^+). The concept of LIBs was first demonstrated in the 1970s by M. Stanley Whittingham using a transitional metal sulphide (TiS_2) as the cathode and Li metal as the anode in contact with a non-aqueous electrolyte. His work showed that Li^+ can be reversibly shuttled between the anode and cathode at ambient temperatures.[3] In comparison to rechargeable batteries based on aqueous electrolytes, the

performance of LIB is much better in terms of both charge stored per volume and weight of the battery as shown in Figure 2-1 below.[4]
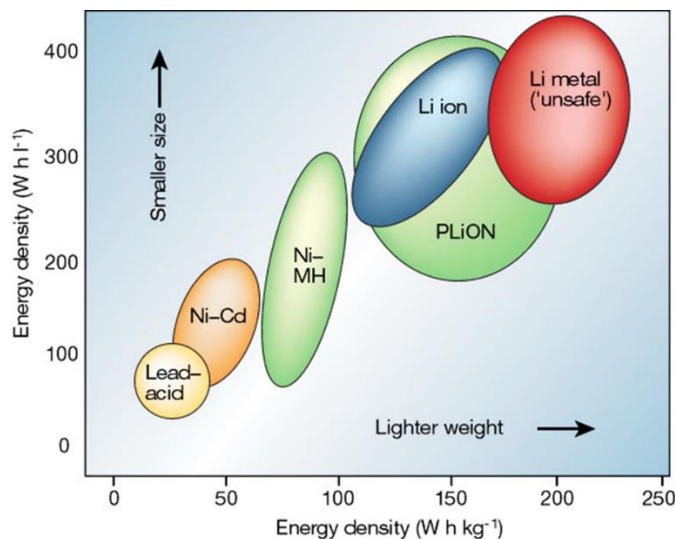
Figure 2-1 Comparison of LIB capacity with other battery technologies (Adapted from ref.[4]).

The properties of Li as an electroactive component of a battery are summarized below:[4–6]

- It is one of the most electrochemically active metal in the periodic table having a low standard reduction potential of -3.04 V vs SHE (Standard Hydrogen Electrode)

- The energy content per each Li electron is the highest for any known solid element

- It has a low molecular weight

- It has a small ionic radius

- It has the lowest density among the group 1 elements

After the discovery made by M. Stanley Whittingham, it was realized that Li metal anode is unsafe for use in LIBs. This is due to the non-uniform redeposition of Li onto the anode. In the long run, this results in the formation of sharp long dendrite that inevitably forms a short circuit with the cathode material.[7] After a few years of optimizing the performance and safety of LIBs, in

1991 the first LIB was commercialized by Sony Energytech.[5] Typical commercial LIBs are composed of thin film layered electrode materials which are graphite (anode) and lithium metal oxide (cathode) in contact with an organic electrolyte. In between the anode and cathode lies a separator (previously soaked in the electrolyte) that prevents electrical contact between both electrodes but permeable to Li^+ from the electrolyte. Typically, copper (Cu) and aluminium (Al) are used as current collectors for anode and cathode, respectively. Cu is used because of its high conductivity and its low reactivity with anode active materials while Al is used due to its high stability, moderate conductivity, and formation of a passivating thin layer of Al_2O_3 that limits corrosion processes. Figure 2-2 illustrates the arrangement of a typical commercial LIB.
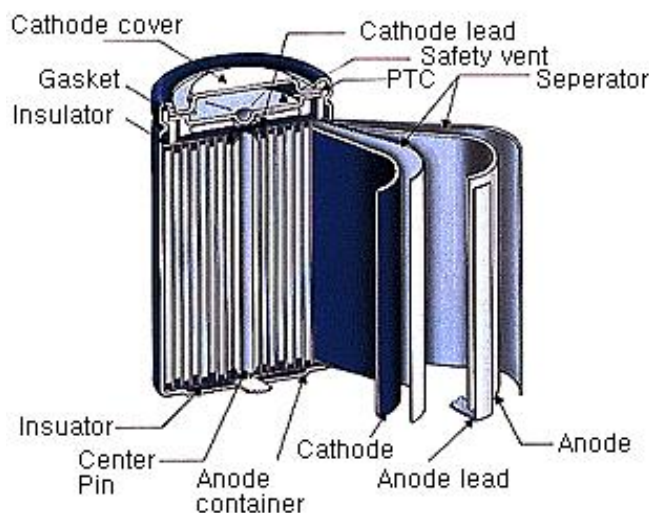
Figure 2-2 Structure of a commercial LIB
(Adapted from ref.[8]).

2.1.1 Mechanism of Charging and Discharging LIBs

Charging of a LIB is achieved when the positive and negative terminal of a direct current power source is connected to the anode and cathode of the LIB, respectively. This connection provides the potential for extracting Li^+ from the interstitial space between the atomic layers within the active material of the cathode and driving it to the interstitial space between the atomic layers

within the active material of the anode through the electrolyte. Such process results in the insertion of Li^+ into the anode in a process commonly termed *lithiation* or *insertion*. At the cathode, the process is termed *delithiation* or *extraction* – which suggests the removal of Li^+. In this context, the anode becomes the negative electrode because it is being reduced by the influx of electrons from the cathode through an external power source while the cathode becomes the positive electrode. Upon discharging the LIB by connecting the anode and cathode to the positive terminal and negative terminal of an external load, respectively, the anode and cathode experience a reversal of polarity. This results in the extraction of dislodged Li^+ in the anode into the cathode and movement of an equivalent number of electrons from the anode to the cathode through the connected external device. The charging and discharging process of a typical LIB is illustrated in the schematic shown in Figure 2-3 while the corresponding chemical equation is presented in equation 2-1, 2-2 and 2-3.[9]
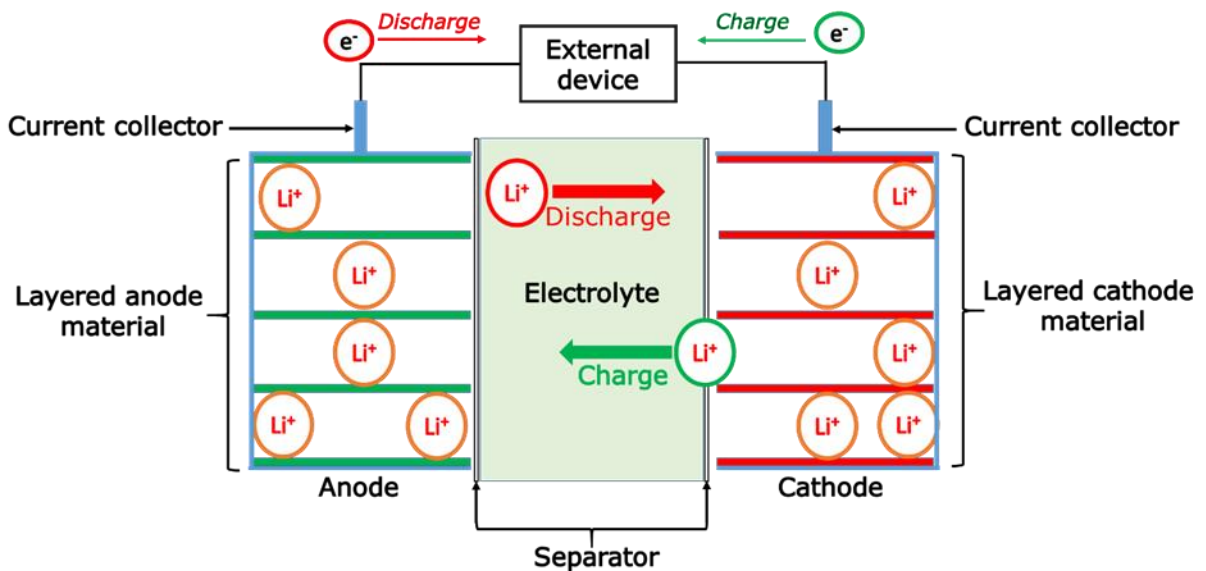
Figure 2-3 Schematic of a LIB in operation.

$$\text{Cathode} \quad LiMO_2 \underset{discharge}{\overset{charge}{\rightleftharpoons}} Li_{1-x}MO_2 + xLi^+ + xe^- \tag{2-1}$$

$$\text{Anode} \quad C + xLi^+ + xe^- \underset{discharge}{\overset{charge}{\rightleftharpoons}} Li_xC \tag{2-2}$$

$$\text{Overall reaction} \quad LiMO_2 + C \underset{discharge}{\overset{charge}{\rightleftharpoons}} Li_{1-x}MO_2 + Li_xC \tag{2-3}$$
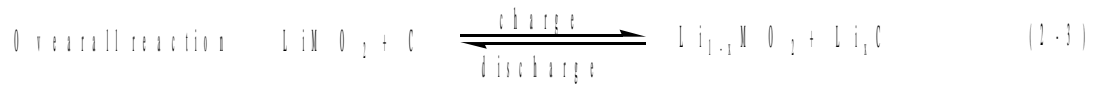
Three mechanisms of dislodging Li^+ into electrodes during usage of LIBs have been identified. These include insertion, alloying and conversion mechanisms. Traditional LIBs anode (graphite) stores Li via insertion. This process guarantees high power density. However, it delivers a limited charge capacity. Some class of materials (notably transition metals) are capable of storing Li by forming a Li-alloyed compound via alloying mechanisms. Prominent examples of such materials are tin and silicon. The resulting Li-alloyed compound is capable of storing larger amounts of Li than insertion-based mechanisms. However, these materials suffer from large volume expansion accompanied by great structural stress during lithiation. This causes them to fracture, thus limiting their cyclability. Another class of materials that are capable of storing Li via phase formation without significant volume change is currently being studied. They undergo a charge storage mechanism termed *conversion*. These materials combine the desirable features of insertion and alloying-based mechanisms. However, they suffer from poor reversibility. Thus, they are rarely used in LIBs.[10] The schematic illustrated in Figure 2-4 describes the type of charge storage mechanisms in LIB electrodes.[7]
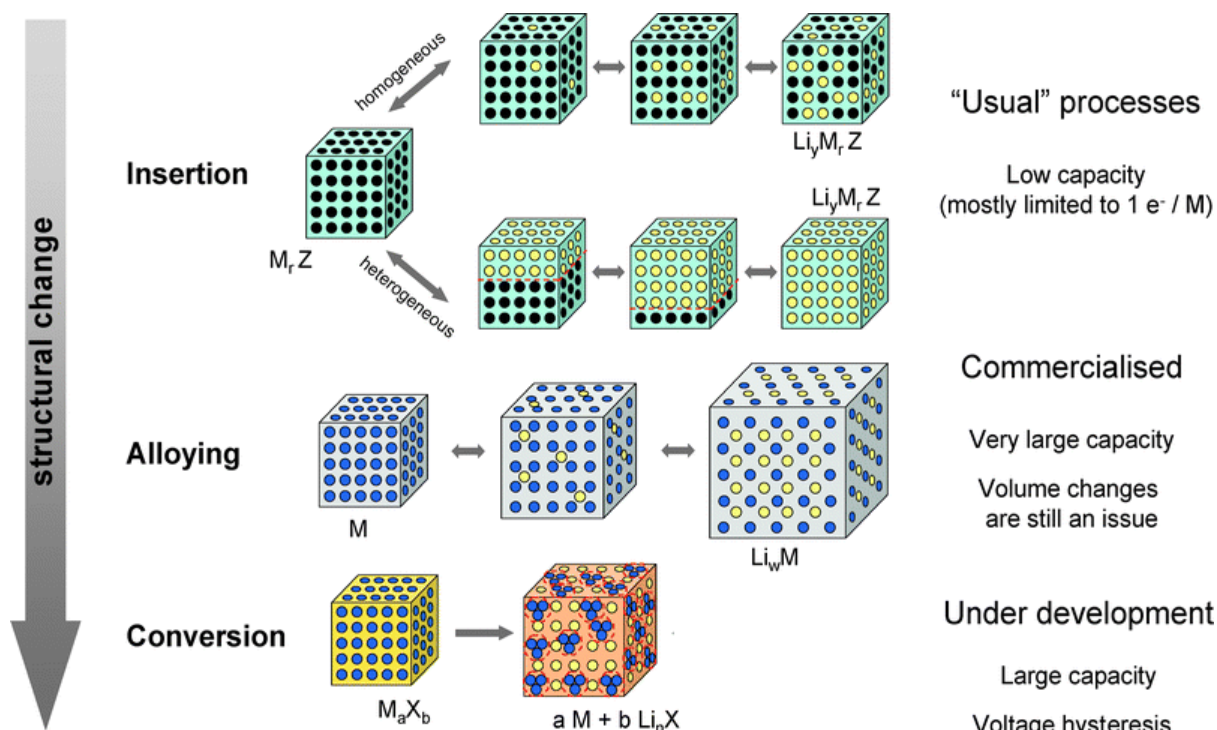
Figure 2-4 A schematic representation of different charge storage mechanisms in electrode materials for LIBs. Black, yellow and blue circles represent void in the crystal structure, lithium and host metal, respectively.
(Adapted from ref.[7]).

2.1.2 Electrode Materials for LIB

There exists a positive correlation between the electronic and ionic energies of a battery material and the resulting performance of a battery, which in turn depends on the battery's open circuit voltage (V_{oc}). In theory, the energy for ionic transfer is dependent on the crystal structure and coordination chemistry of the sites where the ion (Li^+) is generated from and inserted to during cycling. In addition, electronic transfer energy of electrons is dependent on the work function of the electrode materials. For stability of the battery electrode, the electrochemical potential of the anode (μ_A) and cathode (μ_B) must lie within the bandgap (E_g) of the electrolyte in order to reduce side reactions of the electrode with the electrolyte which result in the formation of a passivating layer known as *solid electrolyte interphace* (SEI) as illustrated in the schematic below.[11]
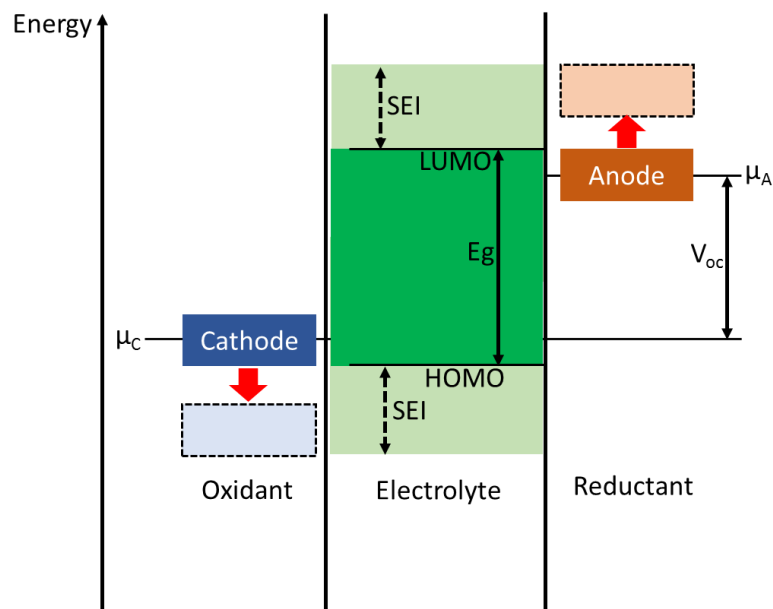
**Figure 2-5 Schematic open-circuit energy diagram of an electrolyte
(Adapted from ref.[11]).**

Mathematically, kinetic stability of the battery is guaranteed if the equation below is satisfied.[11]

$$eV_{oc} - \mu_A - \mu_C \leq E_g \tag{2-4}$$

Where *e* is the magnitude of electronic charge.

For cells with μ_A greater than the lowest unoccupied molecular orbital (LUMO) of the electrolyte or μ_C lesser than the highest occupied molecular orbital (HOMO) of the electrolyte, the formation of SEI is required to stabilize such electrode. Also, equation 2-4 explains why organic electrolyte are commonly used in place of aqueous electrolyte for designing cells not limited to batteries owing to their higher bandgap.[2]

As explained in the previous section, thermodynamic consideration of the electrode materials for battery design plays a critical role in the performance of a battery. The general requirement for candidate materials for LIB electrodes are highlighted below:[9]

- The electrochemical potential of the intercalation material must be well correlated with that of lithium

- The intercalation material must be capable of accommodating large amounts of Li^+ ions into its interstitial spaces

- The structural properties of the intercalation material must be high enough to accommodate mechanical stress during repeated insertion and extraction into its interstitial spaces

- The intercalation material must be conductive enough for electrons and Li^+ in order to reduce polarization loss during usage

- The intercalation material should be chemically stable within the entire voltage window of the electrolyte

- The electrochemical potential of the intercalation material should lie within the band gap of the electrolyte

- In addition, the electrode material should be non-toxic, lightweight, eco-friendly and cost effective

2.1.3 Cathode Materials

Materials for LIB cathode are typically intercalation materials in the form of Li-based alloy or composites as transition metal oxides, transition metal chalcogenides or metal polyanions with olivine, spinel or tavorite structures.[11] In practice, the potential of the cathodic materials must be higher than that of Li. During battery operation, the cathode provides the required Li^+ for storing and generating electrical energy. Compared to the anode, Li storage capacity of cathodes are lesser, hence the performance of a LIB is limited by the capacity of the cathode material.[10] Similarly to anode materials, cathode materials are capable of storing Li via insertion, alloying or conversion

mechanisms but the insertion mechanism still represents the major Li storage process in LIB cathode materials including anodes. Early LIBs used $LiNiO_3$ as the cathode material owing to its higher lithiation as shown in Figure 2-6.[4,12] The use of $LiNiO_3$ was however discontinued due to safety reasons arising from exothermic reaction of delithiated $LiNiO_3$ structure with organic electrolyte being used.[4] Common example of present day cathode materials for LIBs includes: $LiCoO_2$, $LiFePO_4$, and $LiMnO_4$ etc.[13]
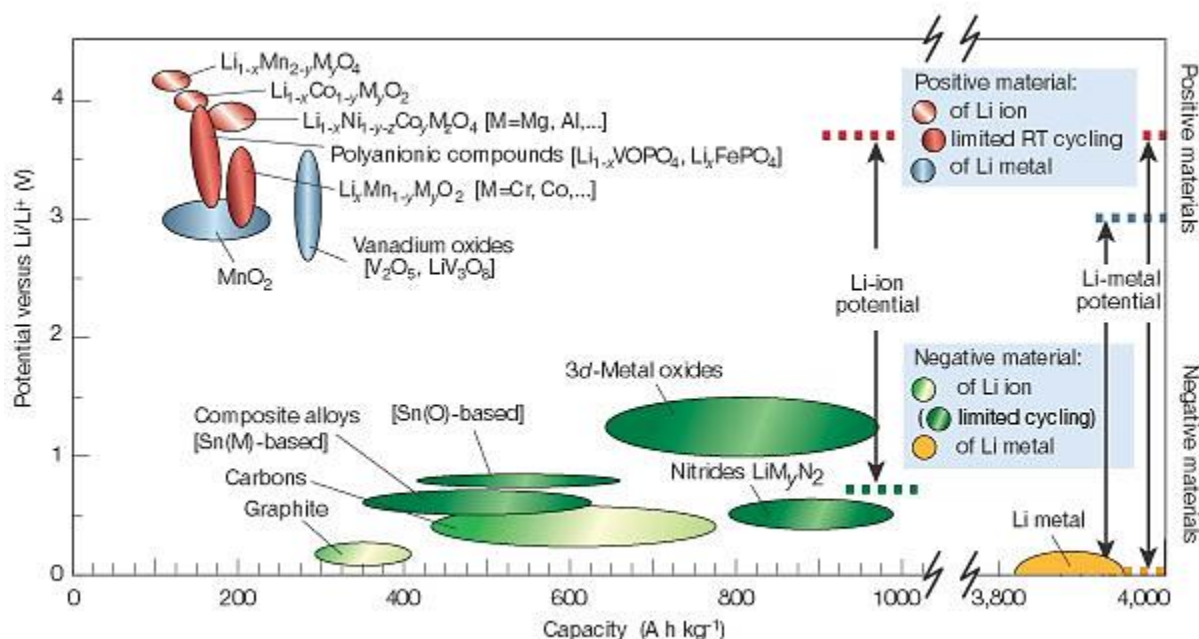
Figure 2-6 The output voltage values of electrode materials for LIBs (Adapted from ref.[4]).

2.1.4 Anode Materials

Graphite still remains the commonly used anode material due to its low lithiation potential, high chemical and thermal stability, low volume changes during repeated usage, good cyclic performance, high abundance and low cost. However, its gravimetric charge capacity is limited to 370 mAh g^{-1}.[14,15] The Li_xC_6 compound forms a passivating surface on graphite (also known as SEI) which prevents the further reaction of graphite with Li^+ from the electrolyte but permeable

16

enough to allow the diffusion of Li into the interstitial space of graphite.[16] For this reason, commercial LIBs cathodes contain an excess amount of Li in order to make up for the Li loss due to SEI formation on graphite and other anode materials during the first cycle charging of the battery. In place of graphite, other polymorphs of carbon not limited to graphene, carbon nanotubes and hard carbon have been investigated but their lower coulombic efficiency and prohibitively high cost limit their use as stand-alone anode materials for LIBs. In light of the remarkable charge capacity offered by anode materials that store Li via alloying mechanism, Si and tin (Sn) have been explored. For comparison, Li-Si alloy has a gravimetric charge capacity of 4200 mAh g^{-1} which is 11 times higher than graphite anodes.[17] However, the large volume expansion of lithiated alloys (which is ca. 296% for Si), which results in the fracture of the electrode still remains a concern. This fractured surface exposes the free active anode material's surface to the electrolyte. For stability purpose, the new exposed area is covered by another SEI at the expense of the anode's intercalated Li$^+$ thus reducing the cycling stability of the cell in the long run. Recently, there has been resurging interest to develop anode materials capable of undergoing conversion reaction during lithiation. A common class of such materials includes lithiated transition metal dichalcogenides. However, their full potential is yet to be realized owing to their capacitive loss due to voltage hysteresis.[10]

2.2 Supercapacitors

Supercapacitors, also known as *electrochemical capacitors* or *ultracapacitors*, are EES devices that convert and stores electricity via accumulation of electrical charges at the electrical double layer interface between its electrodes and electrolyte. Early reports on the development of supercapacitors date back to 1957 when General Electric disclosed the design of an electrolytic capacitor with exceptionally high capacitance.[18] The device comprises a pair of porous carbon

electrodes submerged in an electrolyte as shown in Figure 2-7. As at then, the charge storage

mechanism of the device was unknown. After successive improvement of early designs, the first

commercial supercapacitor was commercialized by Nippon Electric Company in 1977.[19]
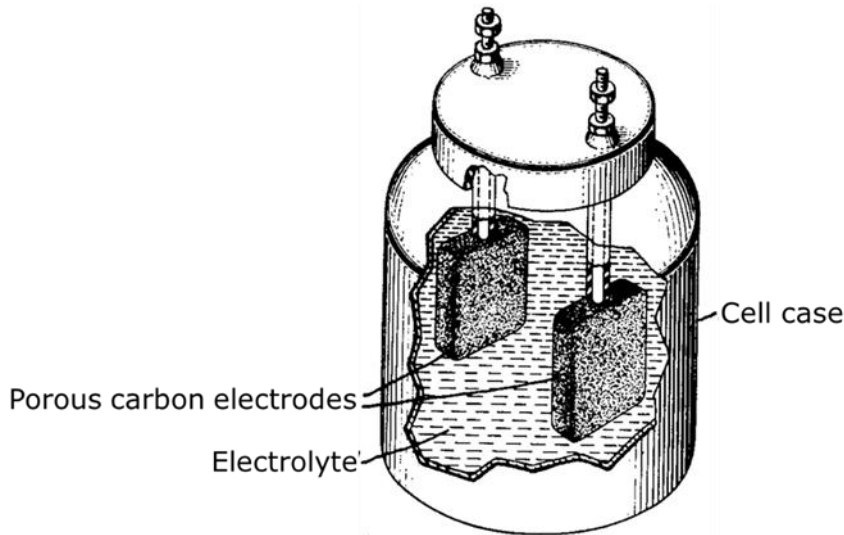
Figure 2-7 Schematic of the capacitor patented by General Electric
(Adapted from ref.[18]).

Typical supercapacitors are composed of two conducting parallel electrodes separated by an

electrolyte. Unlike capacitors, supercapacitors are composed of thin electrodes with a very high

surface area. More so, the distance of separation between the electrodes is kept as small as possible.

2.2.1 Mechanism of Charge Storage in Supercapacitors

Charge storage in supercapacitors is governed by principles that are very similar to that of

conventional capacitors. In capacitors, charge storage is achieved when a potential is applied

across its parallel plates separated by an insulating dielectric material. This results in the

polarization of static charges from a dielectric followed by the build-up of static charge on the

surface of the electrodes as shown in Figure 2-8.
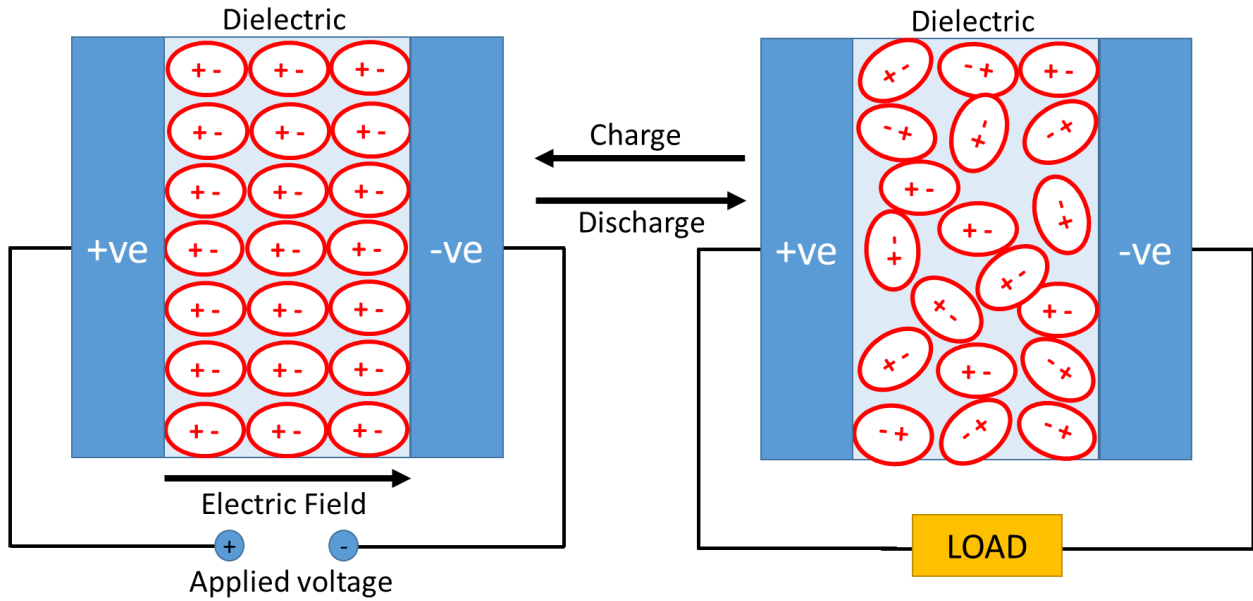
Figure 2-8 Schematic of a working capacitor.

Unlike capacitors, supercapacitors store charges at the interface between conducting electrodes and electrolyte. The accumulated charge forms a layer comprising of two regions known as the *electric double layer*. The inner region (also known as the *Stern layer*) consists of strongly adsorbed ions at the electrode-electrolyte interface while the outer diffused region consists of oppositely charged ions from the electrolyte that are attracted by ions in the Stern layer. The model for this charge storage is known as the *double-layer model* and was first proposed by Helmholtz for explaining the double-layer effect observed in a special class of supercapacitors known as *electric double layer capacitors* (EDLC) and also estimating their capacitance value. This model has been improved till what it is today - as illustrated in Figure 2-9.[20]
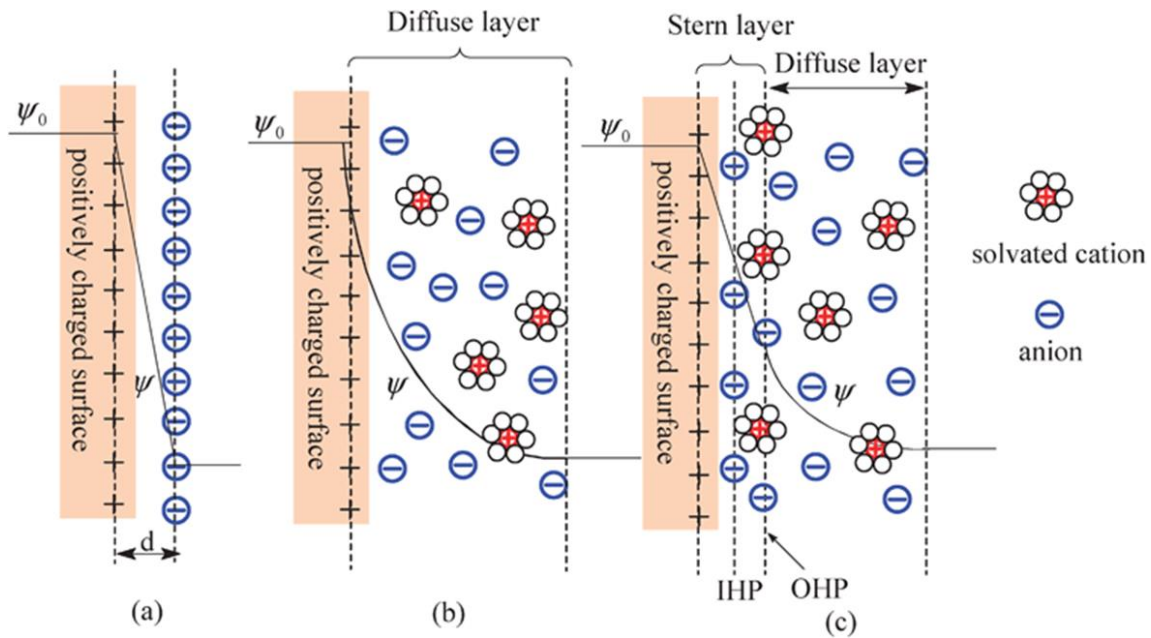
Figure 2-9 Models of the Electrical double layer at positively charge surface according to: (a) the Helmholtz, (b) the Gouy-Chapman model, and (c) the Stern model, showing the inner Helmholtz plane (IHB) and outer Helmholtz plane (OHP) (Adapted from ref.[20]).

Today's supercapacitor consists of two parallel plates conductor separated by a membrane that prevents the physical contact of the electrodes yet, permeable to ions from the electrolyte – as illustrated in Figure 2-10. Similar to batteries, the electrolytes in supercapacitors are impermeable to electrons, rather, they force electrons through the external circuit to the device where they do useful work.[20]
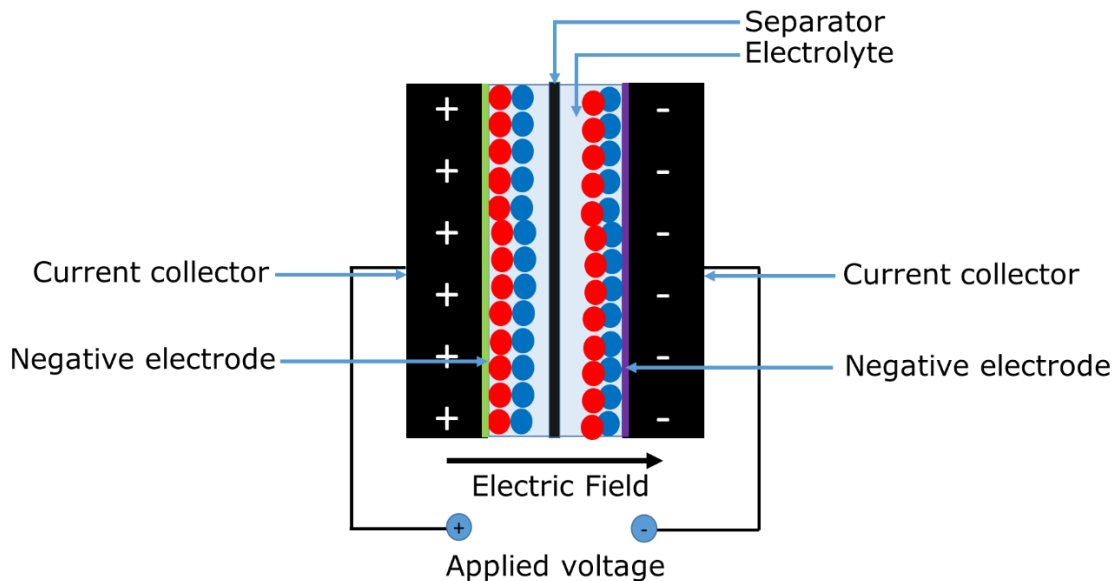
Figure 2-10 Schematic of a charged electric double-supercapacitor.

In addition to charge storage via double-layer effect as observed in EDLCs, another class of supercapacitors known as *pseudocapacitors* also exist. Pseudocapacitors are capable of storing charges at the surface of their electrodes via reversible charge transfer between the electrode and the electrolyte in a process known as *Faradaic reaction*. Common examples of faradaic processes include redox reactions, electrosorption, and intercalation.[21,22] Previous studies have shown that the presence of faradaic process in pseudocapacitor may enhance their capacitance.[22]

2.2.2 Electrode Materials for Supercapacitors

Carbonaceous materials are widely used in the construction of commercial supercapacitor electrodes.[20] Like capacitors, they store charges via physical processes also referred to as *Non-faradaic processes*. However, they demonstrate a higher capacitance due to charge storage via formation of an electric double layer at each electrode. In commercial supercapacitors, carbonaceous materials form an important class of supercapacitors known as the *electric double layer capacitor* (EDLC). Because the charge storage process of EDLCs involves a physical

21

process, their charge storage is highly reversible with remarkable stability. However, their charge storage capacity is lower than that of pseudocapacitors. Typical examples of materials for EDLC electrodes are activated carbons, carbon nanotubes (CNTs), carbon aerogels, and graphenes. The success of commercializing EDLCs lie in their high surface area, lower cost and the preponderance of well-established methods for manufacturing carbonaceous materials compared to other electrode materials.

The quest for improving the charge storage capacity of EDLCs lead to the discovery of pseudocapacitors. Materials for pseudocapacitors are generally classified in two namely: transition metal oxides (TMOs) and conducting polymers. TMOs store charges via sorption of protons into their microstructures. Initial studies on TMOs as electrode materials for supercapacitors focused on ruthenium oxides due to their high conductivity, good stability and low internal resistance when in their hydrous state. However, the prohibitive cost of ruthenium oxides limits their commercialization.[21] Presents studies on TMOs have been focused on phase change manganese oxides due to their low cost and high charge storage capacity. In conducting polymers, the charge storage occurs due to the presence of conjugated carbon structures consisting of alternating single and double bonds. With these conjugated structures, conducting polymers store charges via an oxidation process known as doping. Unlike carbonaceous materials, conducting polymers store charges throughout the bulk of their film, hence they are capable of achieving higher capacitance. However, the instability of the electroactive sites on their polymer backbone reduces their cyclic performance (which is lower than those of EDLCs).[23] Typical examples of conducting polymers that have been studied in this regard includes polyaniline, polypyrrole and polythiophene.[22,23]

Other class of materials for supercapacitors include composites such as those containing carbonaceous materials integrated with conducting materials. It is believed that a combination of

charge storage via faradaic and non-faradaic processes could be achieved with these materials, hence improving their capacity. Composites belong to a special class of supercapacitors known as *hybrid supercapacitors*.[24] Other types of hybrid materials include asymmetric supercapacitor (which contains a combination of EDLC and pseudocapacitor-type electrode), battery-type supercapacitor (which combines a battery electrode and a supercapacitor electrode).[25,26] The classification of supercapacitors based on electrode material types is illustrated in Figure 2-11.
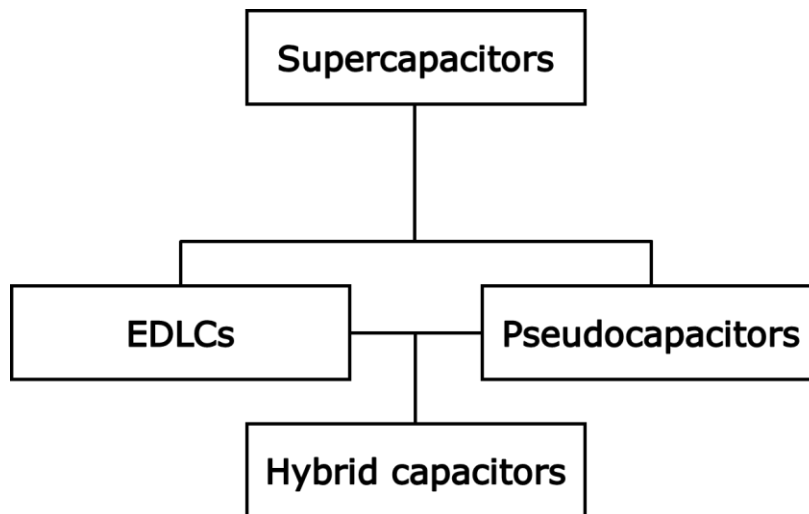
Figure 2-11 Hierarchical classifications of supercapacitors based on electrode -material type.

2.2.3 Metrics for LIBs and Supercapacitors

The capacity of batteries including LIBs is measured in ampere-hour (Ah). The Ah is the total quantity of charge a battery can deliver in an hour before its voltage drops to zero. In practical batteries, charge capacity is measured in specific capacity as mAh g^{-1} (milli-ampere-hour per gram unit) or mAh l^{-1} (milli-ampere-hour per litre). In supercapacitors, including capacitors, the charge capacity is measured in farad (F). Unlike supercapacitors, the capacitance of capacitors is measured in a lower subunit of milli farad (mF) and micro farad (μF). A farad is the storage

capacity of a capacitor/supercapacitor when one coulomb of electricity increases the potential between its electrodes by 1 V. In the scientific community, the capacitance of supercapacitors is reported as specific capacitance in unit of F g^{-1} (farad per gram), F cm^{-2} (farad per square centimeter) or F m^{-3} (farad per cubic meter). One standard metric for comparing the performance of one EES device with another is the energy and power density. The energy density is the amount of charge an EES device can store per unit size. Its units are watt-hour per kilogram (Wh kg^{-1}) or watt-hour per cubic meter (Wh m^{-3}). The power density is the rate at which an EES device can release energy. Its units are watt per kilogram (W kg^{-1}) or watt per cubic meter (W m^{-3}). In comparison, batteries are capable of achieving higher energy density than supercapacitors due to their redox charge storage process. However, batteries possess relatively lower power density and shorter life cycle than supercapacitors. The comparative performance of EES device is typically presented in a plot known as the *Ragone plot* – as shown in Figure 2-12.[1]
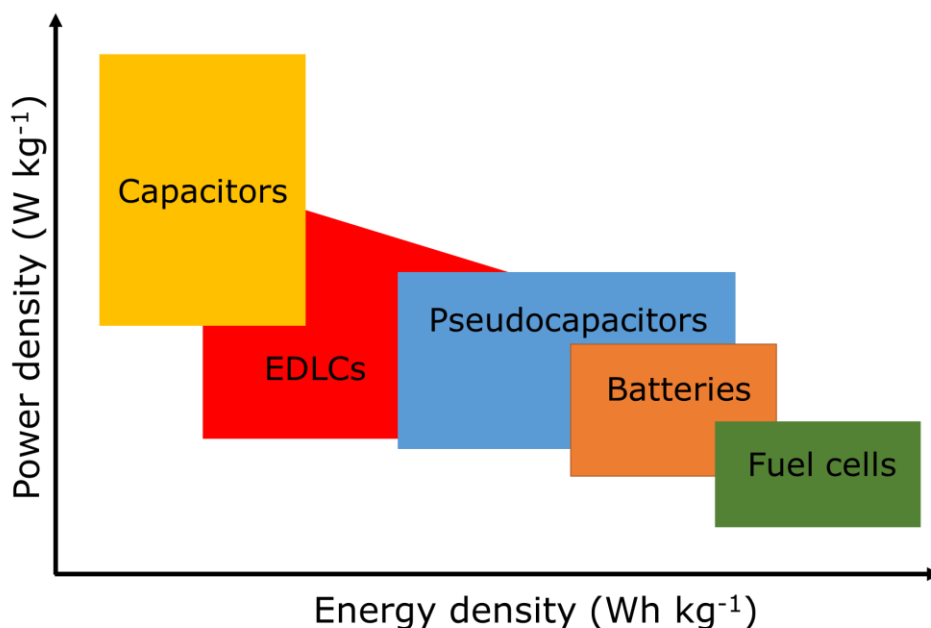
Figure 2-12 Simplified Ragone plot of different electrochemical energy systems (Adapted from ref.[1]).

Another metric for comparing the performance of batteries is the coulombic efficiency (C.E), a measure of the amount of available usable energy of a cell compared to that used for charging the cell. The C.E is calculated as a ratio expressed in percentage. A comparative parameter of supercapacitors and batteries is summarized in Table 2-1.[26]

Table 2-1 A comparison of key performance of batteries and supercapacitors

Parameters	Battery	Supercapacitor
Charge Time	0.3 – 3 h	1 – 30 s
Discharge Time	1 – 5 h	1 – 30 s
Energy Density (Wh kg^{-1})	20 – 100	1 – 10
Power Density (W kg^{-1})	50 – 200	1000 – 2000
Cycle Life	500 – 2000	>100000
Charge/Discharge Efficiency (%)	70 – 85	90 – 95

2.2.4 Polymer-Derived Ceramics

Polymer-derived ceramics (PDCs) are a type of functional ceramics that are prepared via thermal conversion of an inorganic liquid polymer to an amorphous ceramic in a controlled atmosphere.[27] Unlike conventional ceramics, PDCs require a lower synthesis temperature. Also, the feasibility of tailoring their properties by adjusting their polymer precursor sets them apart from other types of ceramics that have been studied in the past.[28] Significant progress in the synthesis of PDCs was made following the work of Fritz and Raabe in 1956 and subsequently that of Yajima *et al*. on the synthesis of SiC ceramic from polycarbosilanes.[27,28] Renewed interest in PDCs began after Verbeek *et al*. reported the polymer-to-ceramic synthesis of Si_3N_4/SiC ceramic fibers from polymer precursors.[29] Since the pioneering work on PDCs, different types of PDCs

have been explored. Generally, PDCs can be categorized according to the number of constituents they contain – as summarized in Table 2-2.[28]

Table 2-2 Classification of PDCs according to their number of substituents

	Type of PDC	Number of constituents	Examples
1	Binary system	2	BN, AlN, SiC, Si_3N_4
2	Ternary system	3	SiCN, BCN, SiOC
3	Quaternary system	4	SiBCN, SiOCB, SiOCAl
4	Pentanary system	5	SiHf(B)CN

The ease of modifying the properties of PDCs by the choice of ceramic precursor and varied processing conditions result in a significant enhancement of their properties such as high thermochemical stabilities, superior mechanical stability, creep resistance and oxidation stability. The combination of the aforementioned properties had made them promising materials for a wide variety of applications not limited to the energy, aerospace, automotive, and biotechnology industry.[28]

In designing materials for EES devices and other applications, a class of PDCS synthesized from organosilicon have gained attention. These PDCs are composed of Si coordinated to a functional group and organic groups as shown in Figure 2-13.[27] Common examples of organosilicon-based PDCs includes SiBCN, SiOCB, SiC, SiOCAl, SiOC etc. The polymer precursor of these ceramics can be readily processed using well-established polymer forming techniques in the plastic industry. However, ternary organosilicon PDCs such as SiOC and SiCN cannot be readily made using conventional starting materials in the polymer industry. They can only be synthesized via polymer-to-ceramic conversion of their precursor under controlled reaction conditions.[28]
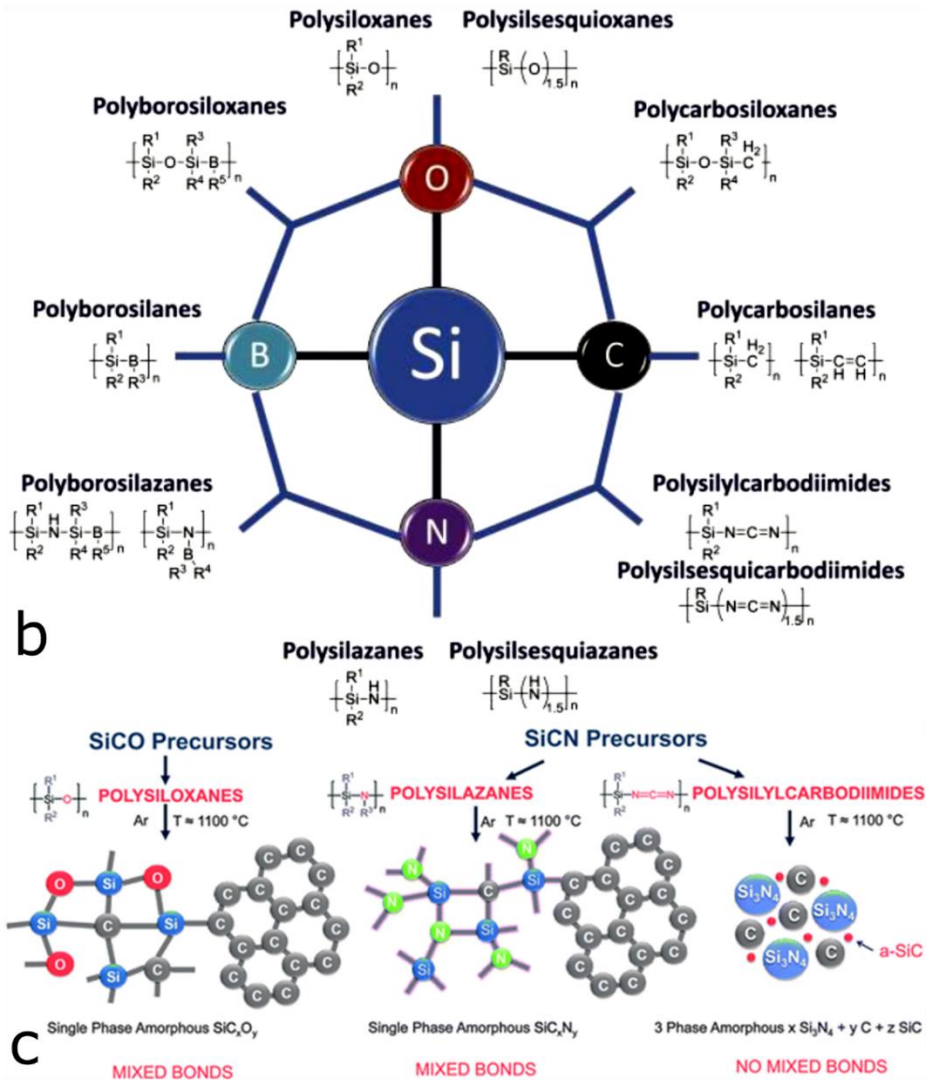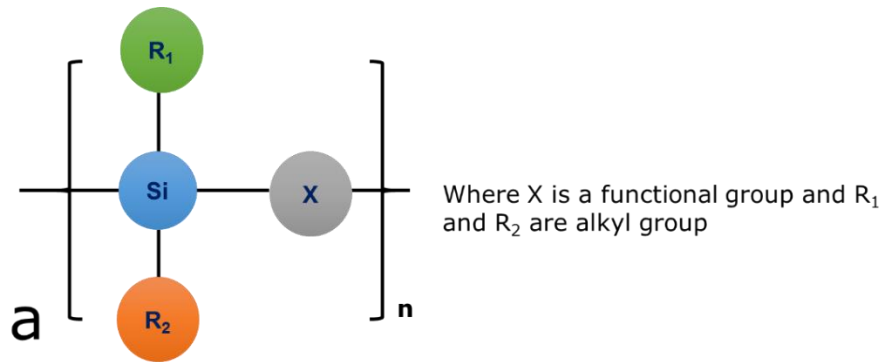
Figure 2-13 (a) Simplified molecular structure of an organosilicon polymer precursor (b) structural forms of different organosilicon polymer precursor (c) structural forms of resulting organosilicon-based PDC
(Adapted from ref.[27, 28, 30]).

2.2.5 Silicon oxycarbide

Silicon oxycarbides are ternary organosilicon PDCs comprising an amorphous tetrahedral network structure of silicate wherein C and O atoms are bonded to Si. SiOC can be represented by a stoichiometric formula of $SiO_{2(1-x)}C_x$ (or $SiO_{4-x}C_x$) + yC (where x ranges from 1 to 4 and y represents the molecularity of the free carbon). Structurally, SiOCs are composed of amorphous silica, SiC and C bonded to Si or itself. However, the existence of C bonded to O is yet to be confirmed.[31] The pyrolysis of their ceramic precursor results in the cleavage C-H bonds, evolution of gases, formation of an amorphous network of SiOC, and randomly distributed free carbons. After pyrolysis, SiOC typically appears as black shiny solids due to the presence non-graphitic (disordered) carbons.[27,32,33]

SiOC with carbon contents exceeding 20 wt.% is termed *carbon-rich*.[28] Such SiOC has a microstructure containing a mixed phase of amorphous $SiO_{4-x}C_x$ and or a silica phase including a free carbon which typically contain amorphous carbon. [27] Carbon-rich SiOCs can either exist as nano-domains when it has a lower amount of free C otherwise, a percolating carbon network.[33]

2.2.6 Synthesis of Silicon oxycarbide

SiOC including other ternary organosilicon-based PDCs are typically synthesized via a polymer pyrolysis route.[34–36] Other methods such as casting,[37] photo-polymerization,[38] hydrosilylation[39] and sol-gel processing[31,40,41] have been reported in the literature but this section will be focusing on the polymer-pyrolysis route used in this thesis. The polymer pyrolysis route involves a two-step process which begins with crosslinking of the polymer and subsequent pyrolysis in a vacuum or in the presence of gases such as argon, nitrogen, and ammonia. Crosslinking of the liquid polymer is done in a temperature range of 100 – 400 ºC.[28] During the

crosslinking step, the liquid polymer is converted to an infusible mass. Afterward, the infusible mass is ball-milled or crushed to obtain fine sized polymer powder. Depending on the intended application of the SiOC, the ball-milled polymer can be processed in various architectures such a fibers (via electrospinning),[42] thin films (via vacuum filtration in a liquid dispersion of graphene oxide) etc.[34–36] Finally, the processed polymer is then subjected to pyrolysis to convert the polymer to a ceramic. This polymer-to-ceramic route for synthesizing SiOC ceramic is illustrated in Figure 2-14. Beyond 1300 °C, phase separation of the ceramic occurs as illustrated in Figure 2-15 and equation 2-5.
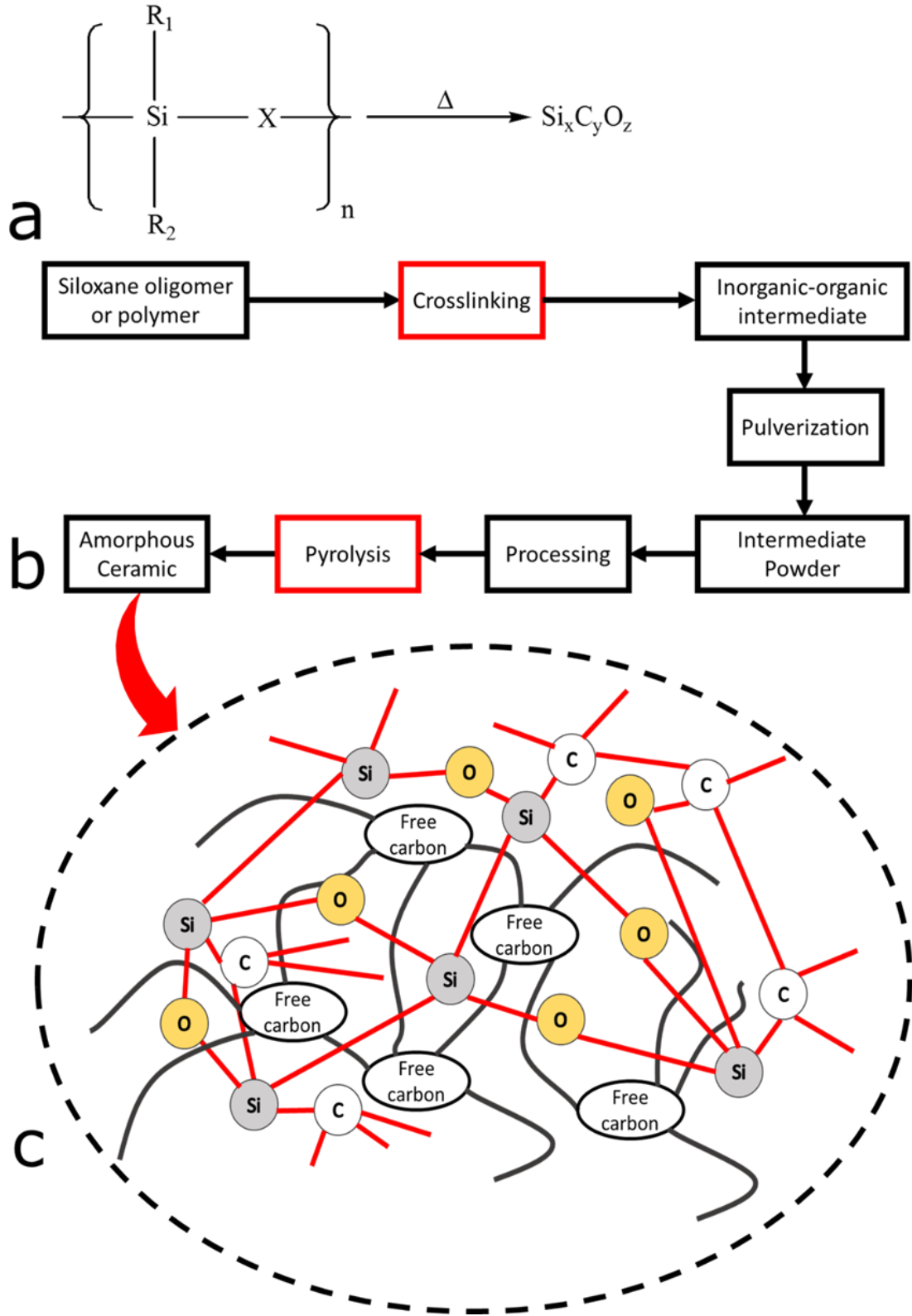
Figure 2-14 (a) Simplified equation for polymer-to-ceramic conversion of SiOC and (b) corresponding steps involved (c) structure of SiOC ceramic showing bond distribution.
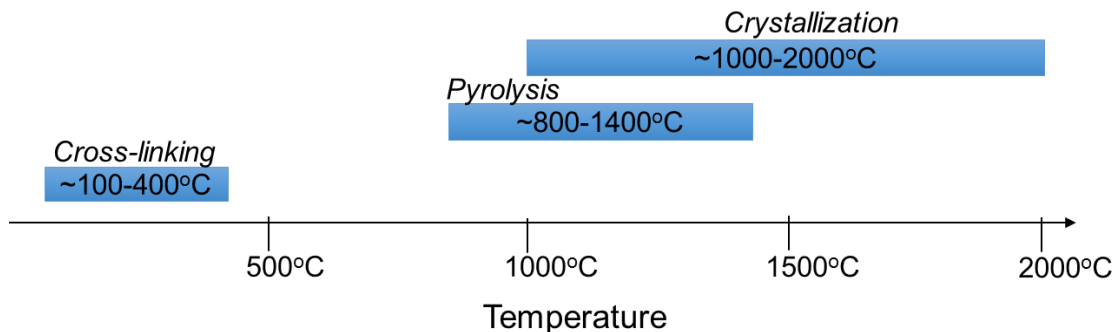
Figure 2-15 Optimal temperature range for polymer-to-ceramic conversion.

2.2.7 Structure of Silicon oxycarbide

In the scientific community, no universally accepted structure of SiOC has been proposed. Pantano *et al*. proposed a structure (Figure 2-16) based on ^{29}Si NMR analyses and ruled out the existence of C-O linkages.[31] Afterward, Scarmi *et al*. [43] and Kleebe *et al*. [44] proposed a model to explain the viscoelastic property of carbon-rich SiOC. This model suggested that SiOC is composed of SiC encapsulated in a graphene-like structure. Upon subjecting SiOC to physical stress (such as those experienced during Li insertion and extraction in LIBs), it returns to its original state without experiencing permanent deformation. Inspired by the findings of Scarmi *et al*., A. Saha *et al*. proposed a model to explain the nano-domain structure of SiOC.[45] This model hypothesize that SiOC is composed of clustered SiO_2 tetrahedral surrounded by SiO_xO_{4-x} and a cage-like connecting path formed by layers of sp^2 graphene – as shown in Figure 2-17.
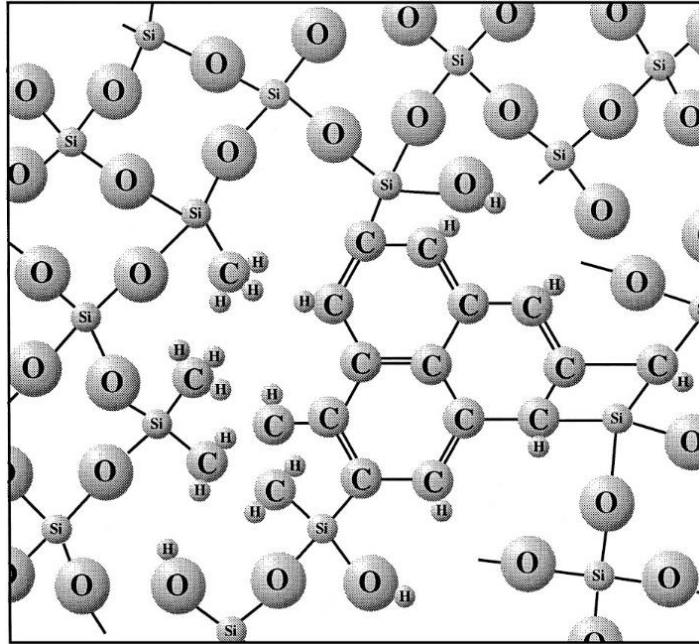
**Figure 2-16 Schematic representation of amorphous SiOC by C.G Pantano *et al.*
(Adapted from ref.[31]).**
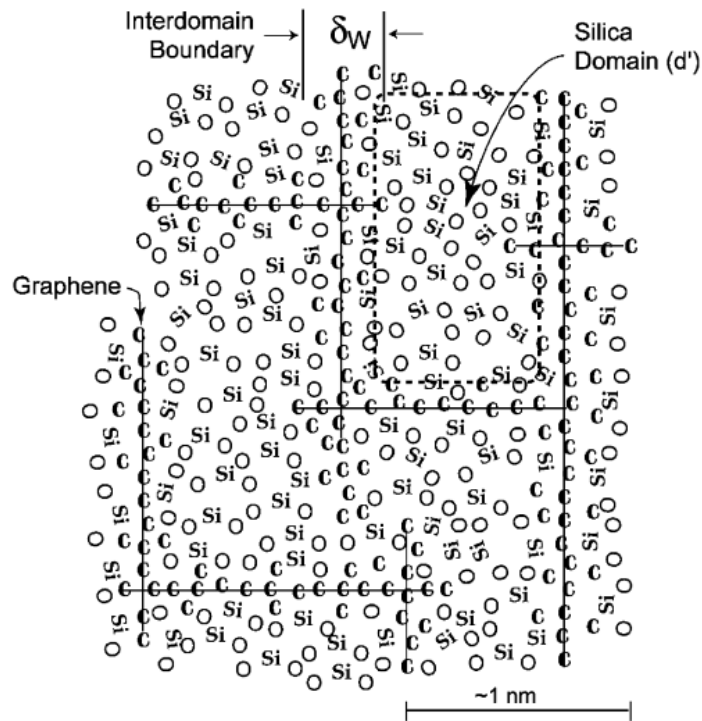
**Figure 2-17 Schematic representation of SiOC nanodomain model proposed by A. Saha *et al*.
(Adapted from ref.[45]).**

2.3 Silicon oxycarbide as electrode material for LIB anodes and supercapacitors

The quest of designing battery electrode materials with high reversible capacity and excellent rate capability have renewed interest in carbonaceous materials containing silicon and other electroactive species. One example of carbonaceous materials that have been considered as anode materials for commercial LIBs is graphite due to its high rate capability, high abundance on earth and low cost. However, its theoretical charge capacity is limited to ca. 370 mAh g^{-1}.[14,15] In view of this, another structural form of carbon containing non-graphitic structures have been explored. Unlike graphite, these carbon structures are composed of disordered carbons arranged in planar hexagonal layers with a short ordering range as illustrated in Figure 2-18. Disordered carbons are formed during pyrolysis of organic compounds below ca. 1500 °C.[46]
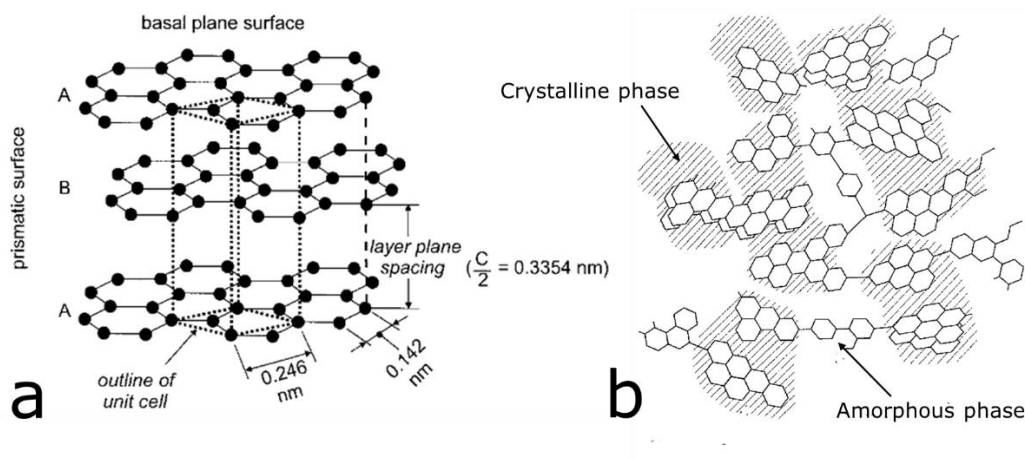
Figure 2-18 Schematic drawing (a) graphitic and (b) non-graphitic carbonaceous material (Adapted from ref.[46]).

In theory, disordered carbons can store a higher amount of Li than graphite and its homologues due to the presence of non-uniform arrangement of their graphene layers which results in stacking faults known for creating additional sites for Li storage. More so, these compounds can

store Li on surfaces and edges of their graphene-like structures. In addition, heteroatom-doping of disordered carbon with Li-active dopants have been reported to improve charge capacity of disordered carbons.[47]

Apart from non-graphitic carbon, Li storage in Si via alloying mechanism have been reported. In comparison, the theoretical charge capacity of Li is ca. 4190 mAh g^{-1}, which is 11 times higher than that of graphite.[17] Like graphite, it is very cheap and eco-friendly. However, Si anodes suffer from volume expansion as high as 295% during lithiation. Cyclic volume expansion of Si anode could cause fracture which eventually would result in the delamination of the active material from the current collector, thus poor performance of the battery.[17]

In view of the shortcomings of graphite and Si-based anodes for LIBs, intense research has focused on designing materials that combines the advantages of both materials which include high charge reversible capacity and excellent capability without significant volume expansion and structural changes. SiOCs including other organosilicon PDCs have become promising materials – as they are known to contain disordered carbon and Si in an amorphous tetrahedral structure.[28,32]

Early studies on the investigation of electrochemical properties of SiOC as anode materials for LIB began in the 1990s when J. R Dahn *et al*. reported Li insertion in pyrolyzed siloxane polymers. This was followed by different studies describing the electrochemical performance of free carbon-rich SiOC in different stoichiometries and configuration as a composite. In light of the feasibility of using SiOC as anode materials for LIBs, further studies have been carried out to characterize its electrochemically active sites. Fukui *et al*. studied the electrochemical properties of carbon-rich SiOC using ^{7}Li magic angle spinning nuclear magnetic resonance spectroscopy (^{7}Li MAS NMR). He proposed that the interstitial spaces and edges of sp^2 graphene layers with SiOC

free carbon phase constitutes the major Li insertion sites. Also, less ionic Li and diamagnetic Li-species could be stored in the micropores and amorphous network of SiOC.[32]

Although SiOC ceramics are promising materials for LIBs anode, however, they suffer a high irreversible first cycle loss and high hysteresis during cycling operation. A combination of factors has been identified as the reason for this capacity loss. These includes:[48]

- Trapping of Li^+ by micropores during initial cycling

- Formation of irreversible Li compounds with dangling bonds (e.g. hydrogen) and oxygen in oxygen-rich sites

In a recent study conducted by V. S. Pradeep *et al.*, it was shown that the pyrolysis temperature of the SiOC precursor plays a significant role in the charge capacity of the resulting ceramic. In their findings, samples pyrolyzed in a temperature range of 800–900 ºC demonstrated higher Li charge capacity. However, the voltage hysteresis of these samples is higher than that of samples pyrolyzed at 1000 ºC and beyond. It was concluded that the disordered free carbon phase in the samples influences the charge storage capacity and reversibility of the pyrolyzed samples. More so, the diminishing charge storage capacity of samples pyrolyzed at 1000 ºC and beyond is due to the loss of free carbon phase as a result of phase separation.[49] The findings of V. S. Pradeep *et al.* is corroborated by J. Kasper *et al.* who concluded that the synthesis of SiOC at higher pyrolysis temperature would result in the graphitization of its free-carbons, thus reducing Li-ion storage capacity. In addition, the gradual phase transformation of Li-active SiOC to inactive SiC also dampens the Li storage capacity of the ceramic.[50]

In an attempt to mitigate the effect of first cycle loss in SiOC, different configurations of the ceramic have been explored. One approach is to synthesize SiOC composites into thin films in order to make it promising for lightweight energy storage applications. Following this rationale,

Bhandavat *et al*. investigated thin film SiOC-CNT composites and reported a charge capacity of ca. 750 mAh g^{-1} at a current density of 50 mA g^{-1}.[51] In another study by David *et al*., SiOC-graphene paper composite demonstrated a remarkable charge capacity of 702 mAh g^{-1} when charged at a current density of 100 mA g^{-1}.[35] Recently, Kolathodi *et al*. investigated the performance of a layer-by-layer SiOC graphene composite and reported a reversible capacity of 750 mAh g^{-1} which stabilizes to 400 mAh g^{-1} at a current density of 50 mA g^{-1}.[36]

As an electrode material for supercapacitor, recent studies have shown that the use of SiOC composites is promising. In this context, SiOC ceramic composites synthesized from different ceramic precursors have been investigated. Kim *et al*. studied the capacitance of SiOC-carbon nanofiber composites and concluded the observed capacitance is due to a synergistic effect between the carbon nanofiber's double layer capacitance and the SiOC's pseudocapacitance.[52] In another study by Meier *et al*., it was reported that a correlation exists between the porosity and capacitance of SiOC-based supercapacitors. However, there exist an optimum porosity beyond which the capacitance of a supercapacitor would diminish. [53] Tolosa *et al*. reported the synthesis of free-standing electrodes made from electrospun SiOC fiber mat. In this study, the free-standing SiOC electrode demonstrated a superior capacity than SiOC electrode materials containing binders. The enhanced capacity of the free-standing electro-spun SiOC fiber was attributed to the absence of binders which are known for diminishing the available pore site for storing ions.[54] Singh and co-workers in another study have demonstrated the capacitive property of a layer-by-layer thin film SiOC reduced graphene oxide (rGO) composite. Their studies concluded that SiOC is capable of being intercalated between the layers of rGO. Thus, improving the available porous site of the composite for charge storage. More so, pseudocapacitive charge storage due to oxygen in SiOC was also noted to improve the capacitance of the composite.[36]

In one of the studies of Singh and co-workers, it was shown that charge capacity of free-standing SiCN-based LIB anodes can be enhanced by interfacing SiCN with boron nitride (BN) nanosheets, a class of insulating ceramic nanomaterials known for their remarkable oxidation resistance, thermal stability, and mechanical properties.[17] The studies reveal that the enhanced Li^+ insertion capacity of SiCN is due to increase in its free carbon when interfaced with BN nanosheets.[6] Inspired by these findings, this thesis investigates the application of an rGO-supported SiOC modified with varying wt.% of boron nitride nanotubes (SiOC-BNNT/rGO) as a material for LIB anode and a symmetric supercapacitor. In the resulting composite, boron nitride nanotubes (BNNT) are expected to suppress SiOC particles against re-aggregation and also enhance the thermal stability and mechanical property of the composites. In addition, rGO would provide conducting path for electroactive species during the electrochemical process and the required mechanical support to synthesize the BNNT-modified SiOC ceramic as a thin film for lightweight electrochemical energy storage applications.[14]

2.4 References

1.   Winter, M. & Brodd, R. J. What are batteries, fuel cells, and supercapacitors? *Chem. Rev.* **104,** 4245–4269 (2004).

2.   Goodenough, J. B. & Park, K.-S. The Li-Ion Rechargeable Battery: A Perspective. *J. Am. Chem. Soc.* **135,** 1167–1176 (2013).

3.   Whittingham, M. S. Lithium batteries and cathode materials. *Chem. Rev.* **104,** 4271–4301 (2004).

4.   Tarascon, J. M. & Armand, M. Issues and challenges facing rechargeable lithium batteries. *Nature* **414,** 359–367 (2001).

5.   Brandt, K. Historical development of secondary lithium batteries. *Solid State Ionics* **69,** 173–183 (1994).

6.   Daniel, C. & Besenhard, J. O. *Handbook of Battery Materials: Second Edition. Handbook of Battery Materials: Second Edition* (2011). doi:10.1002/9783527637188

7.   Palacín, M. R. Recent advances in rechargeable battery materials: a chemist's perspective. *Chem. Soc. Rev.* **38,** 2565 (2009).

8.   Cook, S. How To Get the Most From Your Lithium Ion Batteries. (2010). at <http://www.tested.com/tech/1366-how-to-get-the-most-from-your-lithium-ion-batteries/>

9.   Dongjoon, A. Electrochemical insertion of lithium into polymer derived silicon oxycarbide and oxycarbonitride ceramics. (University of Colorado at Boulder, 2010). at <Retrieved from http://search.proquest.com.er.lib.k-state.edu/docview/504852781?accountid=11789>

10.   Liu, C., Neale, Z. G. & Cao, G. Understanding electrochemical potentials of cathode materials in rechargeable batteries. *Mater. Today* **19,** 109–123 (2016).

11.   Goodenough, J. B. & Kim, Y. Challenges for Rechargeable Li Batteries. *Chem. Mater.* **22,** 587–603 (2010).

12.   Dahn, J. R., von Sacken, U., Juzkow, M. W. & Aljanaby, H. Rechargeable LiNiO2 Carbon Cells. *J. Electrochem. Soc.* **138,** 2207–2211 (1991).

13.   Dou, S. Review and prospect of layered lithium nickel manganese oxide as cathode materials for Li-ion batteries. *Journal of Solid State Electrochemistry* **17,** 911–926 (2013).

14.   Park, J. K. *Principles and applications of lithium secondary batteries*. (Wiley-VCH, 2012).

15.   Aricò, A. S., Bruce, P., Scrosati, B., Tarascon, J.-M. & van Schalkwijk, W. Nanostructured materials for advanced energy conversion and storage devices. *Nat. Mater.* **4,** 366–77 (2005).

16.   Zhang, W. J. A review of the electrochemical performance of alloy anodes for lithium-ion batteries. *J. Power Sources* **196,** 13–24 (2011).

17.   Ashuri, M., He, Q. & Shaw, L. L. Silicon as a potential anode material for Li-ion batteries: where size, geometry and structure matter. *Nanoscale* **8,** 74–103 (2015).

18.   Howard I Becker. Low voltage electrolytic capacitor. (1954).

19.   Balakrishnan, A. & Subramanian, K. R. V. *Nanostructured ceramic oxides for supercapacitor applications*. (CRC Press, 2014).

20.   Zhang, L. L. & Zhao, X. S. Carbon-based materials as supercapacitor electrodes. *Chem. Soc. Rev.* **38,** 2520 (2009).

21.   Conway, B. E. Transition from 'Supercapacitor' to 'Battery' Behavior in Electrochemical Energy Storage. *J. Electrochem. Soc.* **138,** 1539 (1991).

22.   Conway, B. E., Birss, V. & Wojtowicz, J. The role and utilization of pseudocapacitance for energy storage by supercapacitors. *J. Power Sources* **66,** 1–14 (1997).

23.   Mastragostino, M., Arbizzani, C. & Soavi, F. Polymer-based supercapacitors. *J. Power Sources* **97,** 812–815 (2001).

24.   Jurewicz, K., Delpeux, S., Bertagna, V., Béguin, F. & Frackowiak, E. *Supercapacitors from nanotubes/polypyrrole composites*. *Chemical Physics Letters* **347,** (2001).

25.   Pell, W. G. & Conway, B. E. Peculiarities and requirements of asymmetric capacitor devices based on combination of capacitor and battery-type electrodes. *J. Power Sources* **136,** 334–345 (2004).

26.   Zhao, X., Sánchez, B. M., Dobson, P. J. & Grant, P. S. The role of nanomaterials in redox-based supercapacitors for next generation energy storage devices. *Nanoscale* **3,** 839–855 (2011).

27.   Mera, G., Navrotsky, A., Sen, S., Kleebe, H.-J. & Riedel, R. Polymer-derived SiCN and SiOC ceramics – structure and energetics at the nanoscale. *J. Mater. Chem. A* **1,** 3826 (2013).

28.   Colombo, P., Mera, G., Riedel, R. & Soraru, G. D. Polymer-derived ceramics: 40 Years of research and innovation in advanced ceramics. *J. Am. Ceram. Soc.* **93,** 1805–1837 (2010).

29.   Verbeek, W. Production of shaped articles of homogeneous mixtures of silicon carbide and nitride. *Ger. Offen., U.S.Patent No. 3853567* **November 8,** 2218960 (Bayer AG) (1973).

30. Greil, P. Polymer Derived Engineering Ceramics. *Adv. Eng. Mater.* **2,** 339–348 (2000).

31. Pantano, C. G., Singh, A. K. & Zhang, H. Silicon Oxycarbide Glasses. *J. Sol-Gel Sci. Technol.* **14,** 7–25 (1999).

32. Fukui, H., Ohsuka, H., Hino, T. & Kanamura, K. Silicon Oxycarbides in Hard-Carbon Microstructures and Their Electrochemical Lithium Storage. *J. Electrochem. Soc.* **160,** A1276–A1281 (2013).

33. Martínez-Crespiera, S., Ionescu, E., Kleebe, H. J. & Riedel, R. Pressureless synthesis of fully dense and crack-free SiOC bulk ceramics via photo-crosslinking and pyrolysis of a polysiloxane. *J. Eur. Ceram. Soc.* **31,** 913–919 (2011).

34. Bhandavat, R. & Singh, G. Synthesis, Characterization, and High Temperature Stability of Si(B)CN-Coated Carbon Nanotubes Using a Boron-Modified Poly(ureamethylvinyl)Silazane Chemistry. *J. Am. Ceram. Soc.* **95,** 1536–1543 (2012).

35. David, L., Bhandavat, R., Barrera, U. & Singh, G. Silicon oxycarbide glass-graphene composite paper electrode for long-cycle lithium-ion batteries. *Nat. Commun.* **7,** 10998 (2016).

36. Kolathodi, M. S., David, L., Abass, M. A. & Singh, G. Polysiloxane-functionalized graphene oxide paper: pyrolysis and performance as a Li-ion battery and supercapacitor electrode. *RSC Adv.* **6,** 74323–74331 (2016).

37. Shah, S. R. & Raj, R. Mechanical properties of a fully dense polymer derived ceramic made by a novel pressure casting process. *Acta Mater.* **50,** 4093–4103 (2002).

38. Liew, L. A. *et al.* Fabrication of SiCN ceramic MEMS using injectable polymer-precursor technique. *Sensors Actuators, A Phys.* **89,** 64–70 (2001).

39. Sorarù, G. D. *et al.* Novel polysiloxane and polycarbosilane aerogels via hydrosilylation of preceramic polymers. *J. Mater. Chem.* **22,** 7676 (2012).

40. Sorarù, G. D., Pederiva, L., Latournerie, J. & Raj, R. Pyrolysis Kinetics for the Conversion of a Polymer into an Amorphous Silicon Oxycarbide Ceramic. *J. Am. Ceram. Soc.* **85,** 2181–2187 (2002).

41. Wilamowska, M., Pradeep, V. S., Graczyk-Zajac, M., Riedel, R. & Sorar??, G. D. Tailoring of SiOC composition as a way to better performing anodes for Li-ion batteries. *Solid State Ionics* **260,** 94–100 (2014).

42. Tolosa, A. *et al.* Electrospinning and electrospraying of silicon oxycarbide-derived nanoporous carbon for supercapacitor electrodes. *J. Power Sources* **313,** 178–188 (2016).

43. Scarmi, A., Soraru, G. D. & Raj, R. The role of carbon in unexpected visco(an)elastic behavior of amorphous silicon oxycarbide above 1273 K. *J. Non. Cryst. Solids* **351,** 2238–2243 (2005).

44.   Kleebe, H. J. & Blum, Y. D. SiOC ceramic with high excess free carbon. *J. Eur. Ceram. Soc.* **28,** 1037–1042 (2008).

45.   Saha, A., Raj, R. & Williamson, D. L. A model for the nanodomains in polymer-derived SiCO. *J. Am. Ceram. Soc.* **89,** 2188–2195 (2006).

46.   Winter, M., Besenhard, J. O., Spahr, M. E. & Novák, P. in *Advanced Materials* **10,** 725–763 (1998).

47.   Wang, S., Kakumoto, T., Matsui, H. & Matsumura, Y. Mechanism of lithium insertion into disordered carbon. *Synth. Met.* **103,** 2523–2524 (1999).

48.   Vallachira, P. S. P. Study of Silicon Oxycarbide (SiOC) as Anode Materials for Li-ion Batteries. (University of Trento, 2013).

49.   Pradeep, V. S., Graczyk-Zajac, M., Riedel, R. & Soraru, G. D. New insights in to the lithium storage mechanism in polymer derived SiOC anode materials. *Electrochim. Acta* **119,** 78–85 (2014).

50.   Kaspar, J., Graczyk-Zajac, M. & Riedel, R. Lithium insertion into carbon-rich SiOC ceramics: Influence of pyrolysis temperature on electrochemical properties. *J. Power Sources* **244,** 450–455 (2013).

51.   Bhandavat, R. & Singh, G. Stable and efficient li-ion battery anodes prepared from polymer-derived silicon oxycarbide-carbon nanotube shell/core composites. *J. Phys. Chem. C* **117,** 11899–11905 (2013).

52.   Kim, C. H. & Kim, B. H. Effects of thermal treatment on the structural and capacitive properties of polyphenylsilane-derived porous carbon nanofibers. *Electrochim. Acta* **117,** 26–33 (2014).

53.   Meier, A. *et al.* Silicon oxycarbide-derived carbons from a polyphenylsilsequioxane precursor for supercapacitor applications. *Microporous Mesoporous Mater.* **188,** 140–148 (2014).

54.   Tolosa, A. *et al.* Electrospinning and electrospraying of silicon oxycarbide-derived nanoporous carbon for supercapacitor electrodes. *J. Power Sources* **313,** 178–188 (2016).

55.   David, L., Bernard, S., Gervais, C., Miele, P. & Singh, G. Facile Synthesis and High Rate Capability of Silicon Carbonitride/Boron Nitride Composite with a Sheet-Like Morphology. (2015).

Chapter 3 Materials, Methods and Instrumentation

3.1 Materials

Sulfuric acid (H_2SO_4, 96.4%), sodium nitrate ($NaNO_3$, 99.2%), potassium permanganate ($KMnO_4$, 99.4%), hydrogen peroxide (H_2O_2, 31.3% solution in water), hydrochloric acid (HCl, 30% solution in water) and ethanol (C_2H_5OH, 99.9%) were purchased from Fischer Scientific. All materials were used as received without further purification.

3.2 Methods

3.2.1 Preparation of boron nitride nanotube-modified SiOC ceramic

The boron nitride nanotube-modified SiOC (SiOC-BNNT) ceramic was synthesized via pyrolysis of 1,3,5,7-tetramethyl 1,3,5,7-tetravinyl cyclotetrasiloxane (TTCS, Gelest, PA) using a similar polymer-to-ceramic procedure that has been reported in the literature.[1] Typically, varying wt.% of boron nitride nanotubes (BNNTs, Sigma-Aldrich) – with respect to the active weight of TTCS – were dissolved in a liquid mix of TTCS and 1 wt.% of dicumyl peroxide (cross-linking agent). The liquid solution was cross-linked at 250 ^{o}C in argon (Ar) (heating rate of 100 ^{o}C h^{-1}) for a duration of 3 h, resulting in the formation of an infusible mass. The cross-linked BNNT-modified TTCS was then crushed into fine powders and pyrolyzed at 1000 ^{o}C for a duration of 10 h in Ar atmosphere resulting in a fine black BNNT-SiOC ceramic powder termed SiOC-BNNT-2 wt.%, SiOC-BNNT-0.5 wt.% and SiOC-BNNT-0.25 wt.% for the 2 wt.%, 0.5 wt.% and 0.25 wt.% BNNT-modified SiOC ceramic, respectively.

3.2.2 Preparation of ceramic composite paper

Graphene oxide (GO) was synthesized via a modified Hummer's method that has been described previously in the literature.[18] A colloidal suspension of GO (20 ml) in 1:1 (v/v) of deionized water and isopropanol (Fisher Scientific) was made by sonicating for 10 min. SiOC-BNNT powders were slowly added to the GO suspension. The resulting composite suspension was further sonicated for 1 h and then stirred for another 6 h. The composite suspension was filtered by vacuum filtration through a 10 μm filter membrane (HPLC grade, Millipore). The composite paper was carefully removed from the filter membrane and then dried. Later on, the dried paper was thermally reduced in an Ar-filled tube furnace at 500 °C for a duration of 2 h. The papers were cut and then used as electrode materials.

3.3 Characterization techniques

3.3.1 Scanning electron microscopy

Scanning electron microscopy (SEM) is an imaging technique that produces an image by focusing a beam of accelerated electrons on a sample. Unlike the light microscope, the SEM can produce higher resolution images of the sample because it uses beam of electrons (instead of light) - which have a much lower wavelength compared to light. The electron beams are produced by an electron gun, accelerated and focused on specific area of the sample by travelling through electromagnetic fields and magnetic lens. When electron beam impinges on a given sample, different signals which includes: secondary electrons, back-scattered electrons, light and X-rays are produced. In SEM, the secondary and back-scattered electrons being produced are detected by a detector and analysed to produce the sample's image.[3]

In this thesis, the sample's surface morphology was analysed using SEM on a Carl Zeiss EVO MA10 system with incident voltage of 5 to 30 kV.

3.3.2 Transmission electron microscopy

Transmission electron microscopy (TEM) is very similar to the SEM in the sense that both imaging techniques uses a beam of accelerated electrons to image a sample. Unlike SEM, the electron beams are transmitted through an ultrathin sample. Because the transmitted electron bears information pertinent to a sample's internal structure, they are magnified and focused onto an imaging device and a detector picks up the signal. Three types of transmitted electrons are generated namely: elastic scattered, inelastic scattered and unscattered electrons. Depending on a sample's required contrast, bright field and dark field images can be generated using unscattered and scattered electrons, respectively. In addition to using TEM to analyse the internal structure of a sample, it can also be used to produce a diffraction pattern of a sample using a TEM imaging technique known as *selected area electron diffraction* (SAED).[4]

In this thesis, the samples TEM images were taken on a Phillips CM100 under an accelerating voltage of 100 kV.

3.3.3 X-ray photoelectron spectroscopy

X-ray photoelectron spectroscopy (XPS) is a surface technique that can be used for the elemental analysis of a sample and also for identification of the chemical and electronic states of the constituent elements. In this technique, the sample's surface is being irradiated by a beam of X-rays in an ultra-high vacuum environment. During analysis, the incident X-rays excite the sample, resulting in the ejection of the sample's inner shell electron. An electron energy analyzer measures the intensity of the photoelectron and difference between the energy of the incident X-

ray and that of the photoelectron (binding energy). Based on this data, the exact elemental composition and states of the sample's elements can be determined.[5]

In this thesis, XPS spectra of the sample was generated on an X-ray photoelectron spectroscopy (XPS, PHI Quantera SXM) using monochromatic Al Kα X-ray radiation.

3.3.4 Magic Angle Spinning Nuclear Magnetic Spectroscopy

The magic angle spinning nuclear magnetic spectroscopy (MAS NMR) is a solid-state NMR used for identifying and studying individual nuclei present in a molecule or compound. Like NMR, MAS NMR analysis of elements in the periodic table is based on the fact that all elements possess at least one magnetically active isotope with a corresponding nonzero nuclear spin (which is greater than ½ in most cases) and nuclear quadrupole moments. In MAS NMR analysis, samples are irradiated with an intense magnetic field, specific nuclei of the solid sample generate resonant electromagnetic field frequency which is typically expressed as the chemical shift (δ). The emergence of characteristic peaks at a particular chemical shift helps to identify the specific chemical groups in a sample including its corresponding chemical environment.[6]

In this thesis, ^{11}B NMR MAS measurement was undertaken at 11.7 T using a Brucker Avance 500 wide-bore spectrometer operating at a Larmor frequency of 160.47 MHz equipped with a 4 mm Bruker probe with a rotor spinning at 12 kHz. The spectrum was referenced using $BF_3(OEt)_2$ (δ= 0 ppm). The spectrum was acquired using a single pulse experiment at 90° with a pulse of 83 µs and a recycle delay of 1 s.

3.3.5 X-ray diffraction

X-ray diffraction (XRD) is a spectroscopic technique that is commonly used for analyzing and characterizing the crystal structure of a sample. An X-ray-irradiated sample produces intense

diffraction peaks corresponding to specific lattice planes of the sample. Peaks are observed in the XRD spectra when constructive interference occurs among the diffracted X-rays. The condition only occurs when Bragg's law (equation 3-1) is satisfied.[7]

$$n\lambda = 2d \sin\theta \qquad\qquad (3\text{-}1)$$

In this thesis, the XRD spectra of the samples was generated using a PANalytical Empyrean X-ray diffractometer operated at room temperature, with Cu Kα radiation ($\lambda = 1.5418$ Å) and nickel filter. The scanning range was 10-80º at step size of 0.0070.

3.3.6 Raman spectroscopy

This is a technique for detecting molecules and studying the structural transformation they undergo during a chemical reaction. In this technique, the sample of interest is irradiated with a monochromatic light (typically a laser) resulting in the polarization of the sample's electron cloud. In this instance, some of the incident light is absorbed by the sample's molecule, excitation to higher vibrational (phonon) states of the molecule occurs. When relaxation of the excited electron to its ground state or lower vibrational energy occurs, emission of a photon in a direction different from that of the incident light occurs in a process termed *scattering*. Only emitted photons that undergo inelastic scattering results in the generation Raman bands, which are used for identifying a sample.[8]

In this thesis, Raman spectra were collected using a He-Ne laser wavelength of 633 nm (laser power of 17 mW) on a confocal Raman imaging system (Horiba Jobin Yvon LabRam ARAMIS).

3.3.7 Fourier Transform Infrared spectroscopy

This technique is used for detecting functional groups present in a material of interest and studying the evolution of structural bonds in such material due to the absorption or emission of infrared spectra. However, only compounds that possess molecular structures which give rise to change in dipole antisymmetric vibration are considered infrared-active. Typically, a molecular vibrational transition occurs when samples are irradiated with a photon of wavelength in the mid infrared range (2.5 - 15.4 μm). These molecular vibrational transitions result in changes in bond length (stretch vibration) and deformations either by bending or twisting. The vibrational transitions are recorded as spectra comprising of a plot of either absorbance or transmittance against wavenumber.[9]

In this thesis, Fourier Transform Infrared spectroscopy (FT-IR) spectra were obtained using an Agilent Cary 630 FT-IR Spectrometer operated in the total attenuated reflectance mode.

3.4 Electrochemical studies and electrode fabrication

3.4.1 Lithium-ion Battery Testing

The pyrolyzed paper composites were made into working electrodes by cutting a 14.3 mm diameter circular film (weight loading varied from 1 to 2 mg cm^{-2}) from the pyrolyzed papers and used as working electrodes in a Li coin cell setup. The electrolyte solution was made by adding a few drops of 1 M lithium hexafluorophosphate (LiPF$_6$) (Alfa Aesar) to a 1:1 v/v mixture of dimethyl carbonate (Sigma Aldrich) and ethylene carbonate (Sigma Aldrich) with an ionic conductivity of 10.7 mS cm^{-1}. A glass separator (diameter of 19 mm and thickness of 25 μm) pre-soaked in the electrolyte solution was placed between the paper electrode (anode) and pure Li metal (counter electrode, 14.3 mm diameter and 75 μm thick, Alfa Aesar). The whole setup (Figure

3-1) was assembled in an Ar-filled glovebox. Electrochemical performance of the coin cell battery was evaluated using a multichannel BT2000 Arbin test unit 198 sweeping between 2.5 V to 10 mV vs Li/Li$^+$ at a current density of 50 mA g^{-1}.
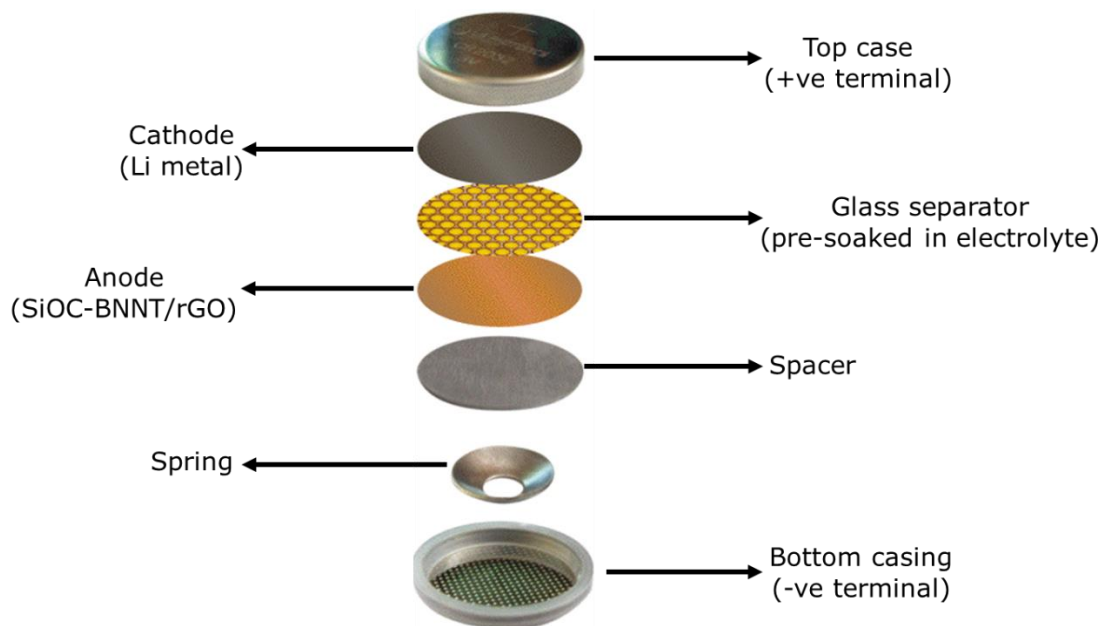
Figure 3-1 Schematic showing the components of a coin cell battery.

3.4.2 Symmetric Supercapacitor Testing

A symmetric two electrode cell configuration (Figure 3-2) was designed to study the electrochemical properties and performance of the paper electrodes as a supercapacitor. The testing was carried out on a CHI660E (CH Instruments, Inc.) electrochemical workstation. The cells were made by cutting a pair of square-shaped electrode materials from the paper electrode and placing a 2 cm x 2 cm Whatman filter paper (serving as a separator) pre-soaked in a 6M potassium hydroxide (KOH, 87.2%, Fisher Scientific) aqueous electrolyte (at room temperature) between them. Cyclic voltammetry (CV) and galvanostatic charge-discharge (GCD) measurements were performed in a potential window of 0 - 0.9 V at different scan rates and current densities,

48

respectively. Electrochemical impedance spectroscopic (EIS) investigation was carried out in the

frequency range of 1 MHz to 10 mHz at open circuit potential with an alternating voltage of 5 mV

amplitude.

Figure 3-2 Schematic showing an assembled symmetric supercapacitor.

3.5 References

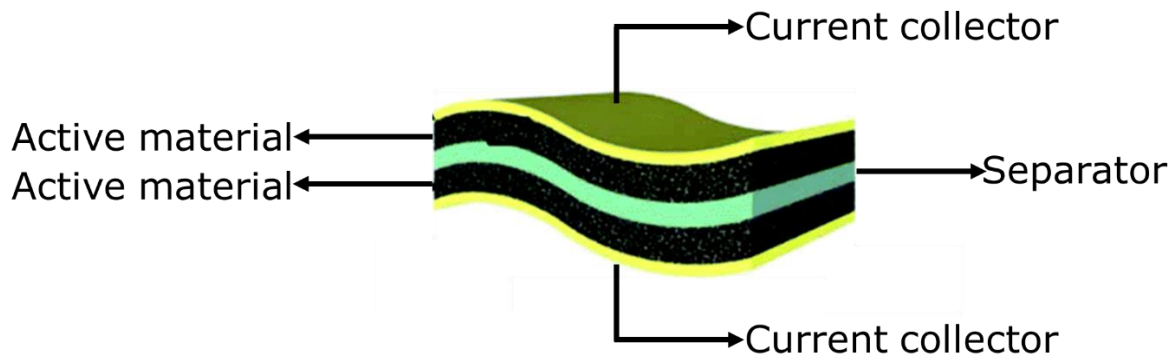1. David, L., Bhandavat, R., Barrera, U. & Singh, G. Silicon oxycarbide glass-graphene composite paper electrode for long-cycle lithium-ion batteries. *Nat. Commun.* **7,** 10998 (2016).

2. Marcano, D. C. *et al.* Improved synthesis of graphene oxide. *ACS Nano* **4,** 4806–4814 (2010).

3. Goldstein, J. I. *et al.* in *Scanning Electron Microscopy and X-ray Microanalysis* 21–60 (Springer US, 2003). doi:10.1007/978-1-4615-0215-9_2

4. Williams, D. B. & Carter, C. B. *Transmission Electron Microscopy: A Textbook for Materials Science*. (Springer Science & Business Media, 2013). at <https://books.google.com/books?id=SAv3BwAAQBAJ&pgis=1>

5. Leng, Y. (Yang). *Materials characterization : introduction to microscopic and spectroscopic methods*.

6. Polenova, T., Gupta, R. & Goldbourt, A. Magic angle spinning NMR spectroscopy: a versatile technique for structural and dynamic analysis of solid-phase systems. *Anal. Chem.* **87,** 5458–69 (2015).

7. Massa, W. *Crystal Structure Determination*. (Springer Science & Business Media, 2014). at <https://books.google.com/books?id=V8ruCAAAQBAJ&pgis=1>

8. Ferraro, J. R., Nakamoto, K. & Brown, C. W. *Introductory Raman Spectroscopy*. *Introductory Raman Spectroscopy* (Elsevier, 2003). doi:10.1016/B978-012254105-6/50000-7

9. Griffiths, P. R. & De Haseth, J. A. *Fourier transform infrared spectrometry*. (Wiley-Interscience, 2007).

Chapter 4 Results and Analyses

4.1 Synthesis of BNNT-SiOC/rGO Composite

Modification of SiOC ceramic with BNNT was achieved via vigorous physical mixing of TTCS with BNNTs. The polymer-to-ceramic conversion of BNNTs-containing TTCS was achieved via pyrolysis in Ar environment. The ceramic powder was crushed into fine powders and then made into a free-standing electrode by vacuum filtration of the fine powders in a dispersion of GO. Heat treatment of the mix resulted in the conversion of GO to rGO. In this context, rGO provides the structural support required to synthesize SiOC-BNNT as free-standing electrodes.

4.2 Morphological and Structural Characterization

4.2.1 Scanning Electron Microscopy

SEM images of the synthesized SiOC-BNNT paper are presented in Figure 4-1. The resulting composite contains chunks (which are believed to be SiOC) with uneven size distribution. Insets a and b in Figure 4-1 shows an enlarged image of the selected section in Figure 4-1. The insets show that the SiOC chunks are dispersed on rGO sheets. In addition, fibrous structure of the BNNTs was retained after pyrolysis. As observed in inset b, BNNTs were embedded in the SiOC-rGO. This configuration is believed to reduce the agglomeration of SiOC, hence enhancing the porosity of the SiOC-BNNT composite paper.
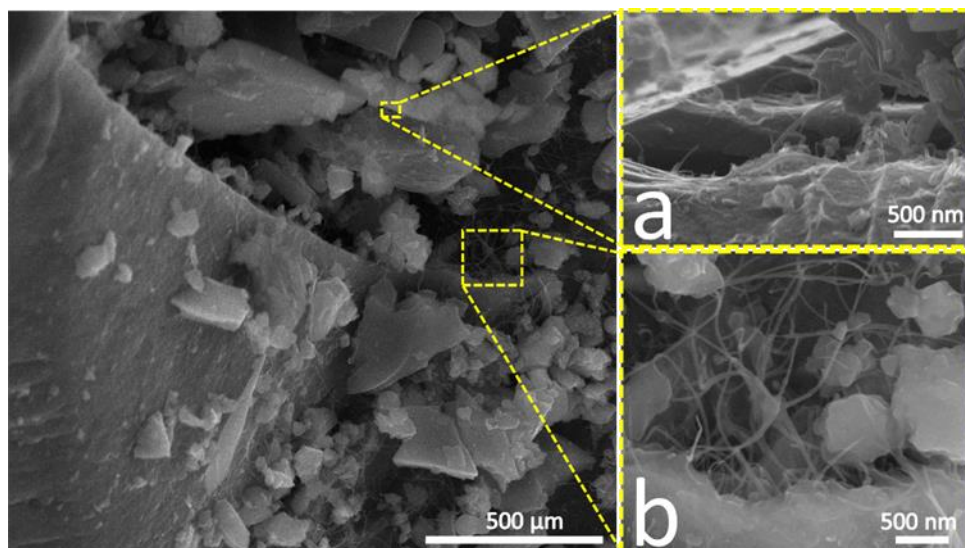
Figure 4-1 SEM images of SiOC-BNNT free-standing paper, insets (a-b) show zoomed images of the regions shown in the main figure.

4.2.2 Transmission Electron Microscopy

TEM images of the SiOC-BNNT paper are shown in Figure 4-2. These images further confirm BNNTs retains their pristine tubular morphology and are embedded in the SiOC-rGO composite (inset b and c). As shown in inset c, the average internal diameter of BNNT dispersed in the ceramic matrix is ~4 nm – which is similar to the internal diameter of the as-received BNNTs. The selected area electron diffraction (SAED) pattern obtained from the red-dotted spots in the image is shown in inset a. The SAED shows diffused concentric rings which are typical of an amorphous material, specifically SiOC in this case.[1]

Figure 4-2 TEM images of SiOC-BNNT paper, inset (a) shows the SEAD image of the area enclosed in red dots, inset (b) shows a section of the tubular BNNT, inset (c) shows the internal diameter of BNNT shown in inset (b).

4.2.3 X-ray photoelectron spectroscopy

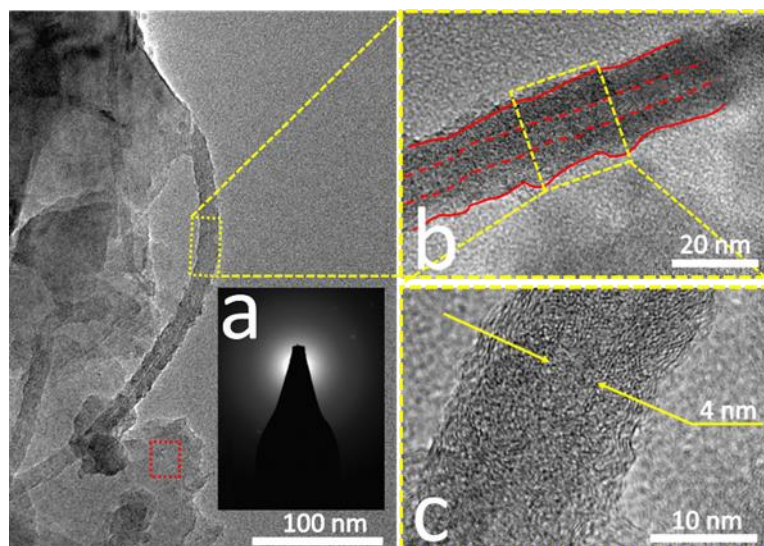The surface elemental composition of the SiOC-BNNT composite was characterized by XPS as shown in Figure 4-3 (a-f). The XPS survey scan (Figure 4-3 (a)) confirms the presence of silicon, nitrogen, carbon, boron and oxygen in the composite. In Figure 4-3 (b), a lower energy peak at 103.21 eV was fitted to Si2p. This peak suggests the presence of Si-O bonds, which is detectable at the surface of the composite.[2] In Figure 4-3 (c), a single peak at 398.64 eV is assigned to B-N for the N1s band.[2] Similarly, a single low energy peak at 191.19 eV (Figure 4-3 (d)) indicating the presence of B-N bonds further confirms the BNNTs in the composite maintains its chemical state after interfacing with SiOC. The high resolution XPS of C1S is displayed in Figure 4-3 (e). Peaks at 284.70 eV, 284.93 eV, 286.58 eV and 288.86 eV could be assigned to C-C (free carbon), C-Si, C=O and CO(O) bonds, respectively.[1] Also, peaks at 532.52 eV and 533.33 eV corresponding to Si-O and SiO_2, respectively were observed in O1S band (Figure 4-3 (f)).[3]
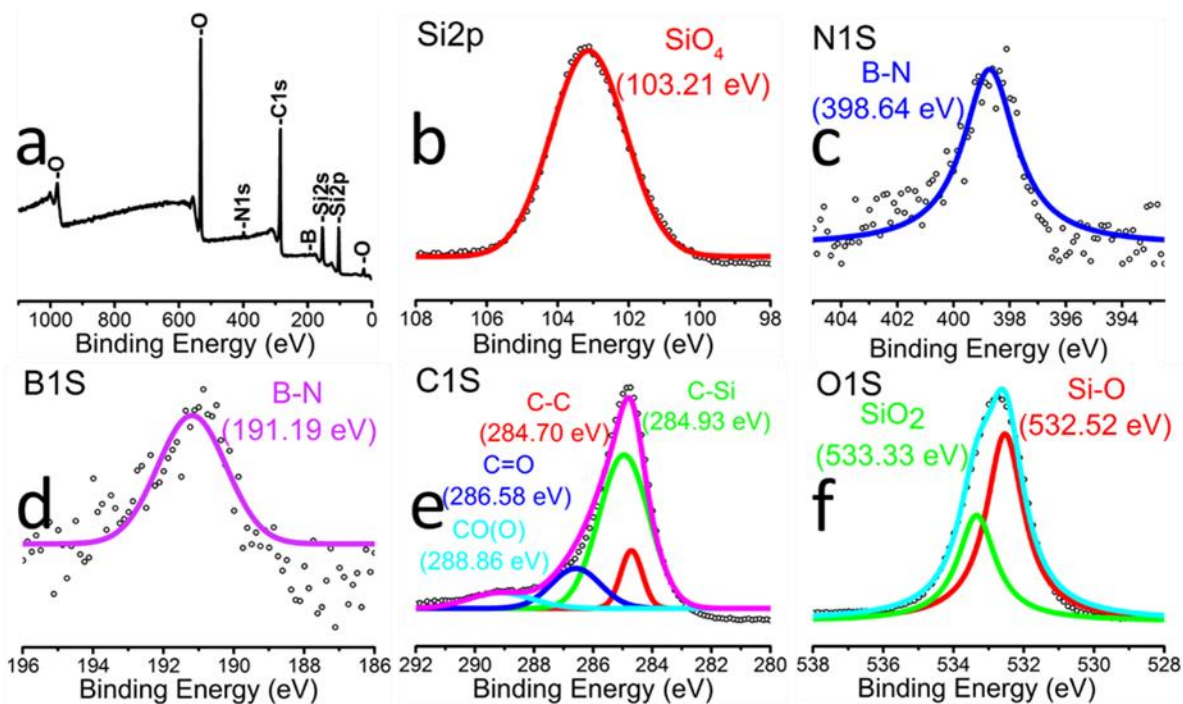
Figure 4-3 XPS showing (a) survey spectrum SiOC-BNNT (b) Si2p (c) N1s (d) B1s (e) C1s (f) O1s.

4.2.4 ^{11}B Magic Angle Spinning Nuclear Magnetic Resonance spectroscopy

The type of boron sites in the synthesized ceramic was investigated using solid-state ^{11}B MAS NMR (Figure 4-4). The spectrum is characteristic of B-N bonds in trigonal BN_3 environments (27 ppm, C_Q = 2.7 MHz, η_Q = 0.2) present in the BNNTs.[3,4] This observation is in agreement with the XPS spectrum of B1s which confirms the presence of BN and absence of tetragonal BO_4 groups in the BNNTs after the polymer-to-ceramic conversion.
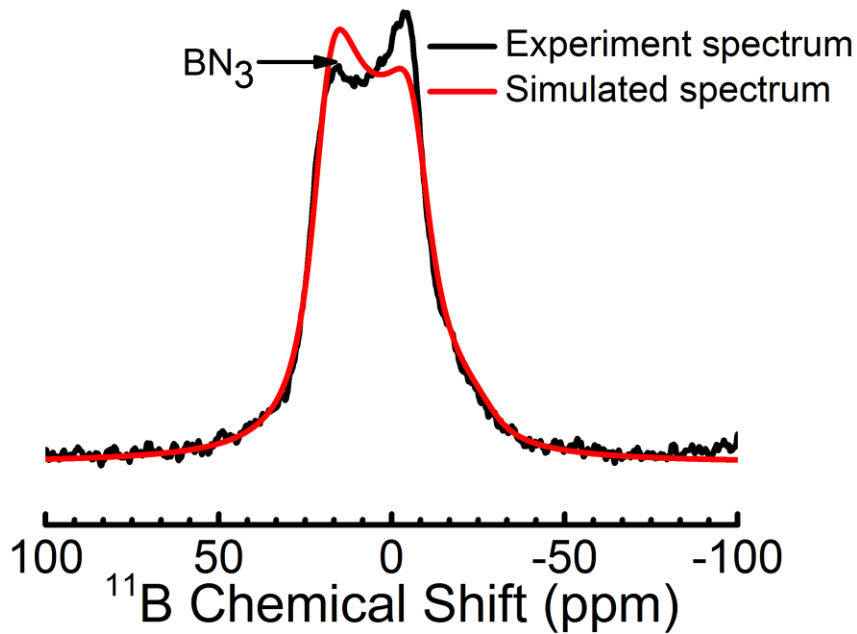
Figure 4-4 ^{11}B MAS NMR spectrum of B in SiOC-BNNT ceramic.

4.2.5 X-ray diffraction

The comparative crystallinity of the cross-linked boron-modified TTCS polymer, SiOC-BNNT, ceramic with that of neat BNNTs is presented in Figure 4-5. Both cross-linked and pyrolyzed specimen displays characteristic 002 peak of BN indicating retention of BNNT within the ceramic's structure after successive heat treatment. In addition, the ceramic sample displays no visible peaks apart from BN 002 peak - which further confirms the SiOC phase in the synthesized composite is amorphous.[3] This observation is in agreement with the SAED diffused concentric ring pattern observed in Figure 4-2 (a).
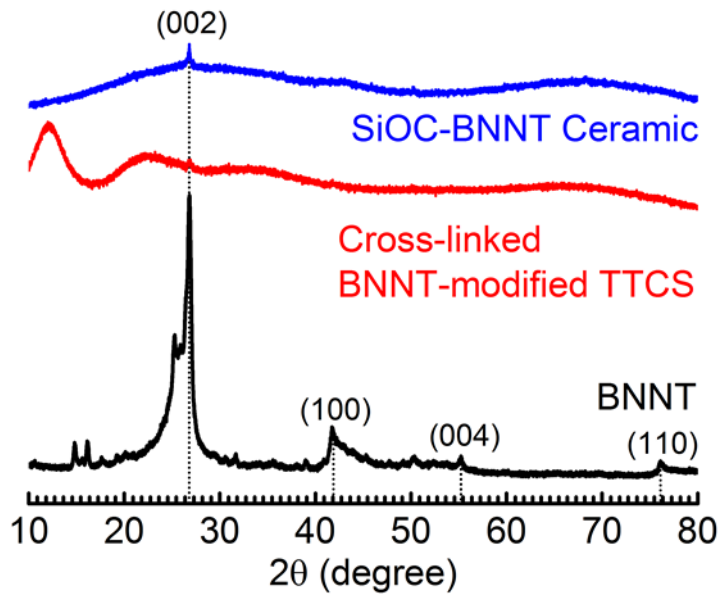
Figure 4-5 XRD peaks of cross-linked TTCS polymer and SiOC-BNNT ceramic in comparison with 'as-obtained' BNNTs.

4.2.6 Fourier Transform Infrared spectroscopy

Structural transformation of the cross-linked polymer (white) to the ceramic (black) was studied using FT-IR spectroscopy (Figure 4-6). The FT-IR spectra of the cross-linked polymer indicates absorption peaks corresponding to Si-OH (3056 cm^{-1}), C-H (2852-2978 cm^{-1}), Si-CH$_3$ (1276-1594 cm^{-1}), Si-O-C (1415 cm^{-1}), Si-O-Si (1037 cm^{-1}), Si-O(C) (791 cm^{-1}) and Si-C (725 cm^{-1}).[1,5-7] Also, characteristic peaks (774 cm^{-1} and 1367 cm^{-1}) due to BN were observed in the cross-linked polymer.[7,8] Polymer-to-ceramic transformation was confirmed by the FT-IR spectra of the ceramic which indicates breaking of bonds corresponding to Si-CH$_3$ and C-H and dampening of prominent Si-O-Si and BN peaks.[6] The only visible bands in the SiOC-BNNT ceramic are those corresponding to Si-H, Si-O-Si, BN and SiC – which further confirms polymer-to-ceramic transformation had occurred. This observation corroborates the decrease in the BN 002 peak intensity shown in the XRD spectra (Figure 4-5). More so, the absence of Si-O-B peaks in the FT-

IR spectra of the ceramic suggests no appreciable chemical reaction had occur between the TTCS polymer and BNNT during pyrolysis.[1]
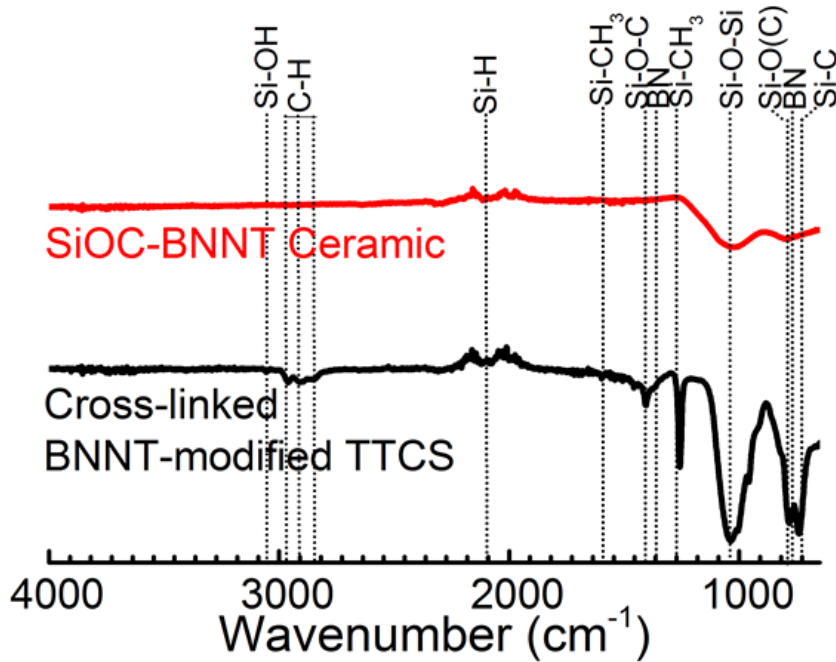
Figure 4-6 FT-IR spectra of BNNT-modified polymer and ceramic.

4.2.7 Raman spectroscopy

In order to study the degree of disordering of the free carbon phase present in the SiOC-BNNT composite at different BNNT interfacing level, Raman spectroscopic analysis was carried out. The Raman spectra of the composite are presented in Figure 4-7. As observed, the composite shows two distinct peaks corresponding to the D and G bands, which are typical of incompletely graphitized carbon atoms in SiOC (disordered carbons).[9] The emergence of the D and G band is believed to be due to disorder-induced vibrations of 6-membered aromatic rings and plane bond stretching of a sp^2 pair of hybridized carbon atoms, respectively.[10] In addition, the Raman spectra revealed a broad D″ band with low intensity, which suggests the presence of amorphous carbon in the SiOC-BNNT samples. Also, the position of the D and G bands shifts towards lower wavenumbers portion of the Raman spectra with an increasing concentration of BNNT in SiOC.

More so, the D to G band intensity ratio (I_D/I_G) was the least for SiOC-BNNT-0.25 wt.% composite. This indicates a lower ordering and size growth of graphite crystals, hence a higher disordered carbon. [11,12]

Figure 4-7 Raman spectra of SiOC-BNNT ceramic with varying wt.% of BNNTs.

4.3   Electrochemical Characterization of SiOC-BNNT

4.3.1 Lithium-ion Battery Test
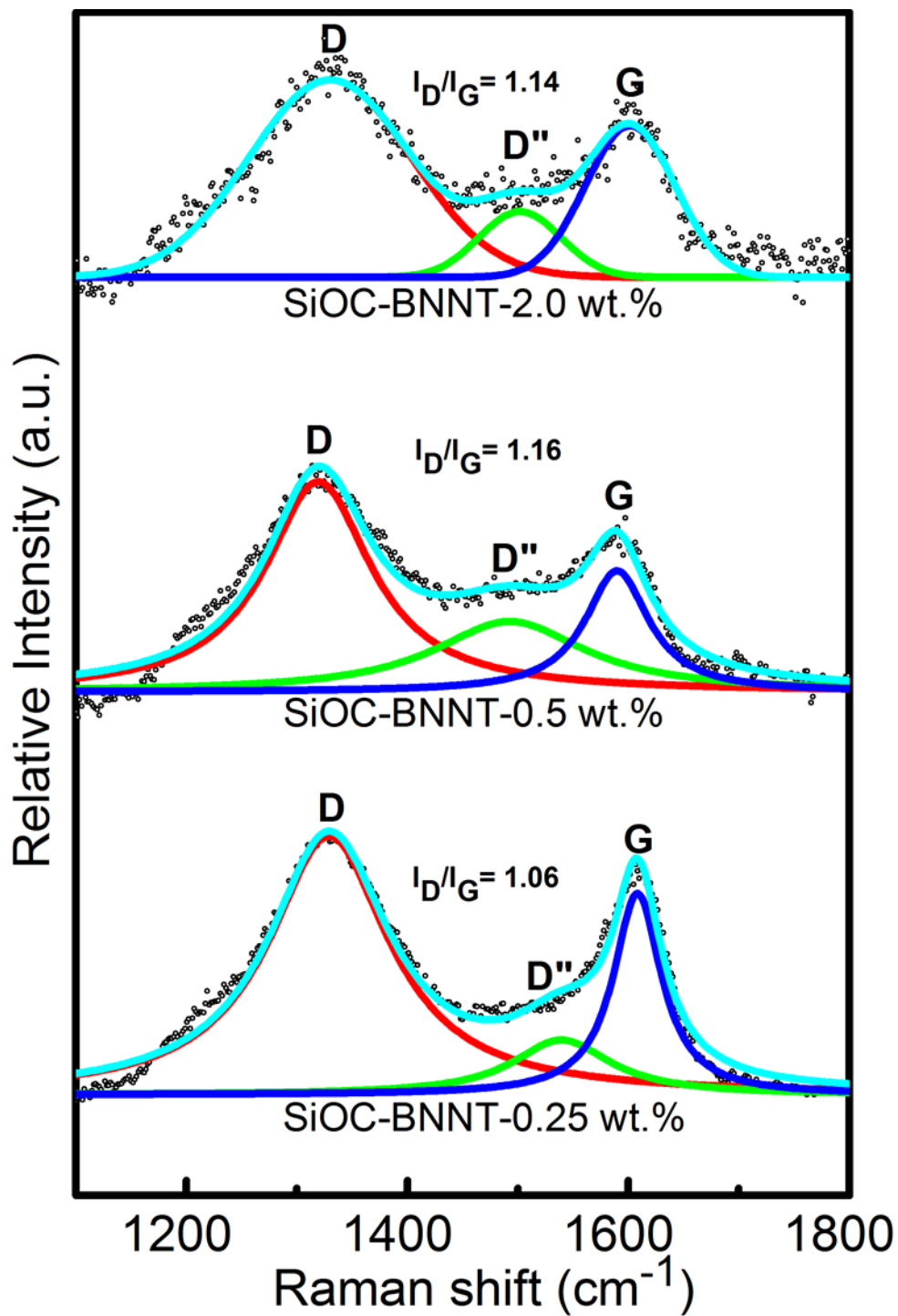
The electrochemical performance of the binder-free SiOC-BNNT composites (containing 40 wt. % of rGO) were tested as anode material for LIBs using a Li half-cell configuration containing a pure Li metal counter electrode. The specific capacity values of the tested materials were calculated with respect to total weight of the electrode material including the active material. The 1st and 2nd cycle charge-discharge profiles of the tested ceramic composite at a current density of 100 mA g^{-1} are presented in Figure 4-8 (a-c). The charge-discharge profile of the tested samples is very similar. When comparing the shape of the 1st cycle discharge profiles, an irreversible capacity near 0.11 V, 0.10 V and 0.12 V corresponding to the 2.0 wt.%, 0.5 wt.% and 0.25 wt.% BNNT-modified ceramic composite, respectively was observed. This irreversible capacity is believed to be due to the formation of solid-electrolyte interphase (SEI) layer.[5] Also, the 1st cycle discharge profile of the tested samples have a long plateau below 0.3 V, indicating an irreversible lithium insertion. Milamowska *et al*. have suggested the observed irreversible voltage plateau is due to the presence of oxygen-rich SiO sites which are known for irreversibly reacting with Li during insertion.[13] The findings of Peter *et al*. on the modeling and Ab-initio simulation of Li insertion in SiOC ceramics have also shown that the enthalpy of Li insertion into oxygen-rich sites in SiOC is very low and are promoted by free carbons, hence the ease of binding Li with these sites. On the other hand, Peter *et al*. also reported that free carbons are also capable of enhancing the reversible storage of Li.[14] In the 2nd cycle, Li insertion capacity of the 2.0 wt.%, 0.5 wt.% and 0.25 wt.% BNNT-modified ceramic composite drops to ca. 369 mAh g^{-1}, 301 mAh g^{-1} and 440 mAh g^{-1}, respectively.

Among the tested ceramic composite paper, SiOC-BNNT-0.25 wt.% demonstrated the highest 1st cycle Li insertion and extraction capacity of ca. 812 mAh g^{-1}and 410 mAh g^{-1}, respectively with a 1st cycle loss of 51%. Table 4-1 summarizes the 1st cycle lithiation capacity (C_{ch}), reversible delithiation capacity (C_{rev}), irreversible capacity (C_{irr}) and corresponding efficiency (η) – where η is calculated using the expression below:

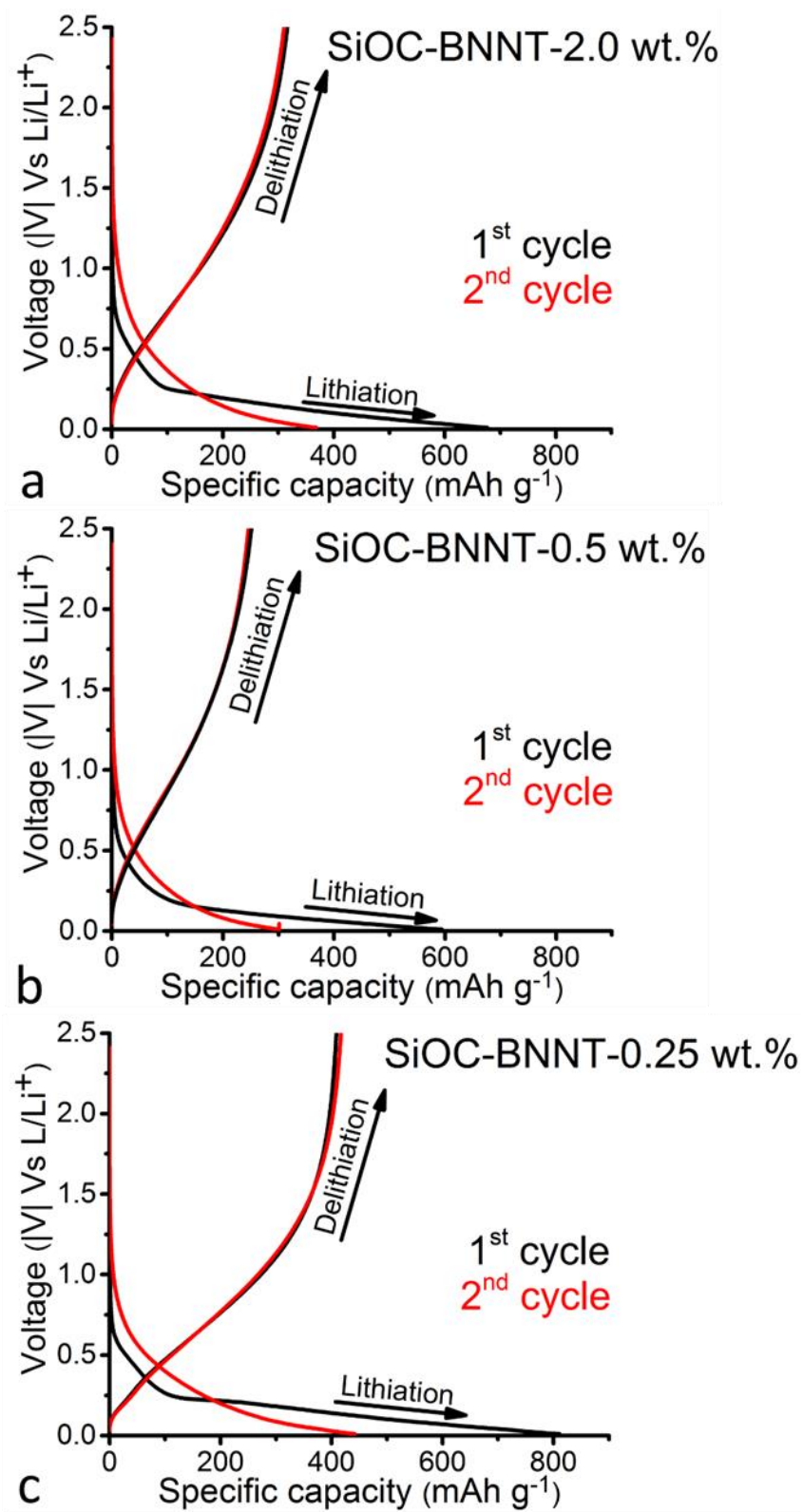$$\eta = C_{rev}/C_{ch} \times 100 \qquad\qquad (4\text{-}1)$$

Figure 4-8 (a-c) 1ˢᵗ and 2ⁿᵈ cycle charge-discharge profile of SiOC-BNNT paper composite.

Table 4-1 Comparison of the 1ˢᵗ cycle lithiation capacity, reversible delithiation capacity, irreversible capacity and corresponding efficiency for SiOC-BNNT/rGO electrodes

Material	C_{ch} (mAh g⁻¹)	C_{dch} (mAh g⁻¹)	C_{irr} (mAh g⁻¹)	η (%)
SiOC-BNNT-2.0 wt.%	317	678	361	46.7
SiOC-BNNT-0.5 wt.%	251	596	345	42.1
SiOC-BNNT-0.25 wt.%	409	812	403	50.4

All tested BNNT-modified ceramic composite paper display significant hysteresis in the 1ˢᵗ cycle as seen in Figure 4-8. The capacity loss during the 1ˢᵗ cycle is attributed to the formation SEI and incomplete conversion reaction during lithiation at the anode.[5,15,16]

The composite ceramics were further cycled asymmetrically by doubling the current density (starting with 100 mA g⁻¹) every 5 cycles. As shown in Figure 4-9, the 0.25 wt.% demonstrated the highest rate performance, which remains at 238 mAh g⁻¹ even at 1600 mA g⁻¹ (after 25 cycles). On the other hand, the 0.5 wt.% and 2.0 wt.% BNNT-modified ceramic composite demonstrated a lithium extraction capacity of 47, and 82 mAh g⁻¹, respectively after 25 cycles. More so, the cyclic efficiency plot shown in Figure 4-9 indicates all tested electrode demonstrates a stable cyclic efficiency when cycled with increasing current density.

So far, SiOC-BNNT-0.25 wt.% remains the best performing electrode material among the BNNT-modified ceramic composite. The observed trend suggests a possible replacement of the oxygen atoms in oxygen-rich sites of SiOC with B which reduces the insertion of Li into SiOC since Li is more attracted to ionic Si-O bonds. On the contrary, studies have shown that ceramics derived from organosilazanes (SiCN) experiences a higher charge capacity when their microstructure is optimally modified with BN nanosheets which result in an increase in the amount of free carbon phase, which serves as active site for reversible storage of Li.[17] Also, it is inferred

that modification of SiOC ceramic with BNNT at higher wt.% could degrade its property due to the insulating property of BN, thus resulting in lower electrochemical performance.[18] Surprisingly, the SiOC-BNNT-2.0 wt.% displays a higher charge capacity than the SiOC-BNNT-0.5 wt.% sample. This disparity is attributed to the higher ordering of graphitic planes in SiOC-BNNT-0.5 wt.%, (as evidenced by the Raman spectra shown in Figure 4-7) thus offering a lesser disordered carbon phase for Li insertion.[12]
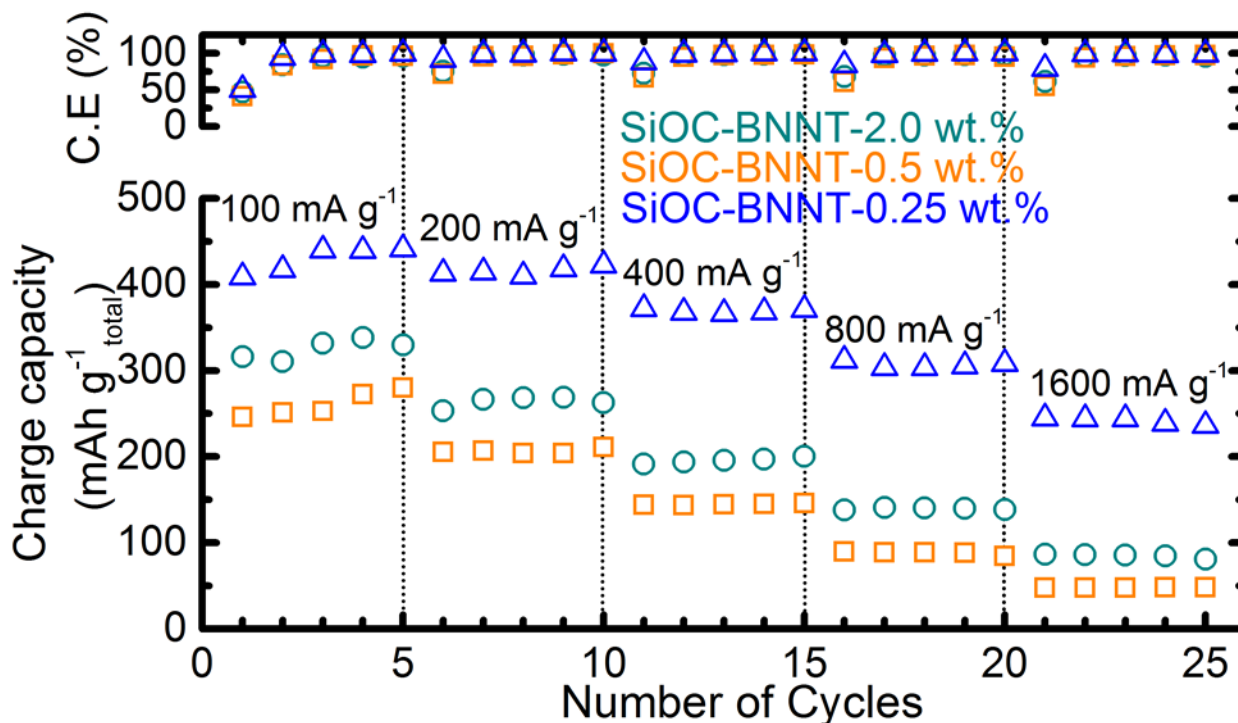
Figure 4-9 Charge capacity of all electrodes asymmetrically cycled at different current densities and corresponding cyclic efficiencies.

4.3.2 Symmetric Supercapacitor Test

The electrochemical performance of the SiOC-BNNT composite paper at varying wt.% of BNNT was analyzed in a two-electrode setup. The testing was carried out in 6M $KOH_{(aq)}$ at room temperature. The cyclic voltammogram (CV), constant current charge-discharge (GCD) and electrochemical impedance spectroscopy (EIS) of the electrode materials are presented in Figure

4-10 (a-c). In the past, it has been shown that neat SiOC supported on graphene sheets is capable of storing charges via faradaic processes due to the presence of oxygen in its structure.[16] The CV curve (at 20 mV s^{-1}) of the SiOC supported on graphene sheets at different concentration of BNNT is presented in Figure 4-10 (a). The electrode materials display a noticeable oxidation peak at ca. 0.5 V – with the SiOC-BNNT-0.5 wt.% displaying the largest oxidation peak. More so, SiOC-BNNT-0.5 wt.% displayed the largest CV area among the tested electrode materials. In this configuration, the SiOC-BNNT-0.5 wt.% has the optimum concentration of BNNT for electrochemical energy storage as a symmetric supercapacitor electrode.

In order to understand the charge-discharge properties of the SiOC-BNNT paper electrodes at constant current, the GCD analysis at a current density of 1 A g^{-1} was carried out (Figure 4-10 (b)). As expected, the GCD profiles of the SiOC-BNNT/rGO electrode materials are not uniform, suggesting the presence of faradaic charge transfer process in the material.[16] Also, the SiOC-BNNT-0.5 wt.% electrode material demonstrates the least steepest discharge slope with a capacitance of 52.96 F g^{-1}. Based on the superior charge-discharge properties of SiOC-BNNT-0.5 wt.%, it can be inferred that higher ordering and size growth of graphitic crystals could result in enhanced electrochemical energy storage. Moreover, the decrease in the electrochemical charge storage performance of SiOC-BNNT-2.0 wt.% is believed to be due to the difficulty in dispersing BNNTs in SiOC at higher concentration.[1]

The electrochemical resistance of the SiOC-BNNT/rGO electrode materials was characterized using EIS. Figure 4-10 (c) shows the Nyquist plots and magnified high-frequency region in the inset. The intercept of the curve with the X-axis in the high-frequency region indicates the interfacial resistance of the cell setup which is believed to be due to the contributing resistance of the electrode material, electrolyte, and current collector.[19] As observed in the magnified high-

frequency region, the SiOC-BNNT-0.5 wt.% sample displays the lowest interfacial resistance with a value corresponding to 0.52 Ω which is comparable to that of SiOC previously reported in the literature.[16] In addition, none of the tested electrode materials display a semicircle in the high-frequency region, suggesting a very low interfacial resistance as a result of the conductive nature of the electrode materials.[20] Also, SiOC-BNNT-0.5 wt.% displays a steeper frequency tail in the low-frequency region which indicates a higher mass transfer of ions between the electrolyte and its pores.[21]
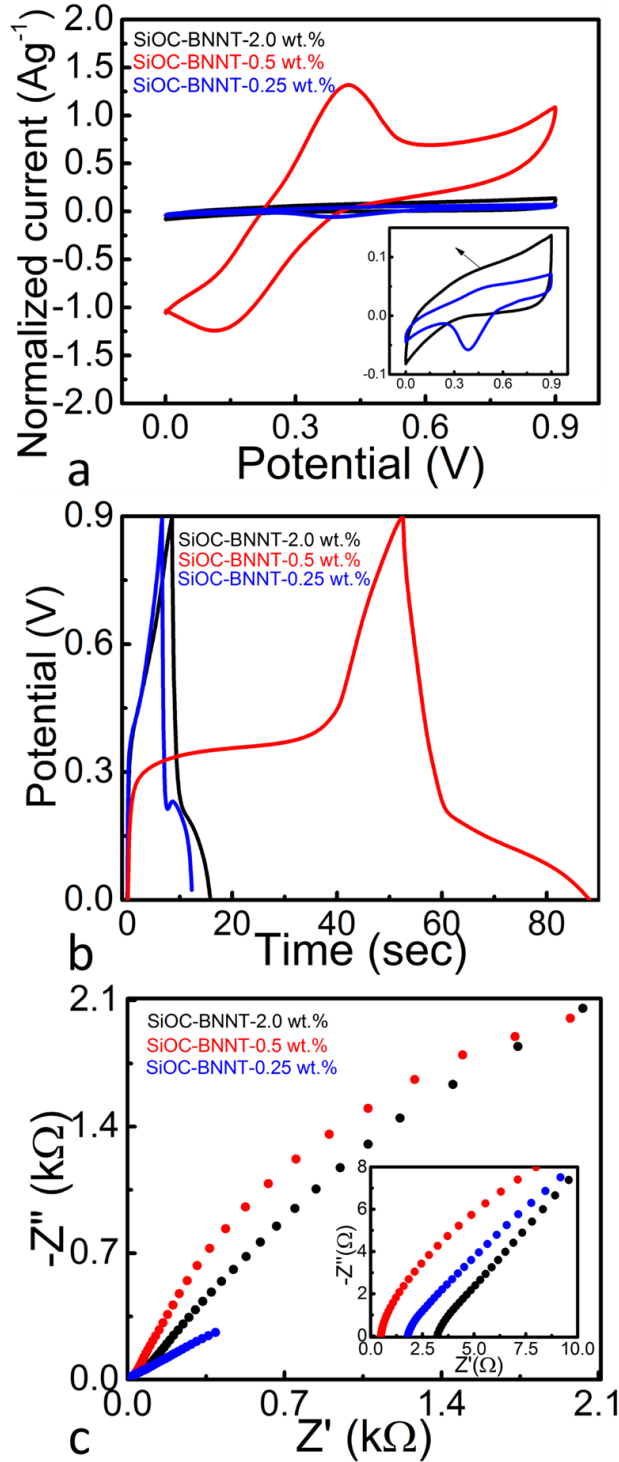
Figure 4-10 (a) Cyclic voltammograms of SiOC-BNNT composite paper at 20 mV s^{-1} (inset shows expanded CV of the 2.0 wt.% and 0.25 wt.% composite paper electrode (b) Galvanostatic charge-discharge curve of SiOC-BNNT composite paper electrode at a current density of 1.0 A g^{-1} (c) Nyquist plots for SiOC-BNNT composite paper (inset shows expanded plot at high frequency region).

Based on the preliminary results from the CV, GCD and EIS of the tested materials, it is evident that the SiOC-BNNT-0.5 wt.% is the best performing electrode material. As observed in the Raman spectra shown in Figure 4-7, the SiOC-BNNT-0.5 wt.% sample has the highest growth size of ordered graphitic planes. However, we are yet to establish the correlation between ordering of SiOC-BNNT/rGO graphitic planes and it capacitance. Further electrochemical characterization was carried out in order to determine the charge storage behavior of SiOC-BNNT-0.5 wt.% as a supercapacitor electrode material.

The SiOC-BNNT-0.5 wt.% was tested using same setup described earlier – wherein the electrode material was made into a symmetric supercapacitor and tested in 6M $KOH_{(aq)}$ electrolyte at room temperature. The CV and GCD plots of SiOC-BNNT-0.5 wt.% are presented in Figure 4-11 (a-b). CV plots of SiOC-BNNT-0.5 wt.% (Figure 4-11 (a)) shows quasi-rectangular plots with broad reduction and oxidation peaks around 0.1 V and 0.4 V, respectively. The relative position of the redox peaks is very similar to that of neat SiOC paper previously reported by our group.[16] As such, it is believed that the charge storage mechanism of SiOC-BNNT composite paper is also faradaic.[22] Also, the CV profile of SiOC-BNNT-0.5 wt.% remains unchanged up to lower scan rates, indicating enhanced electrode-electrolyte interaction which translates to higher charge storage performance. Corresponding GCD plots presented in Figure 4-11 (b) show a similar non-linear charge-discharge profile that has been observed in layer-by-layer SiOC-rGO, which is in agreement with the CV plots shown in Figure 4-10 (a) – suggesting the SiOC-BNNT-0.5 wt.% composite paper is pseudocapacitive.[16] The specific capacitance of SiOC-BNNT-0.5 wt.% was calculated from the GCD plot shown in Figure 4-11 (b) using equation (4-2).

$$C_s = 2I\Delta t \, /m\Delta V \qquad\qquad (4\text{-}2)$$

Where Cs, I, Δt, m and ΔV represent the specific capacitance (F g^{-1}), current (A), discharge time (sec), mass (g) and voltage window (V, excluding IR drop during discharge process), respectively.

At a current density of 1.0 A g^{-1}, SiOC-BNNT-0.5 wt.% displays a capacitance of 78.93 F g^{-1}. In an attempt to evaluate the cyclic performance of SiOC-BNNT-0.5 wt.%, its cyclic stability was studied. Figure 4-11 (c) presents the cyclic stability of SiOC-BNNT-0.5 wt.% after 185 cycles at a current density of 1.5 A g^{-1}. The cyclic retention was 86% with a corresponding specific capacitance of 26.67 F g^{-1} – which is comparable to that of some carbonaceous materials that have been reported in the literature.[23,24] Yet, lower than neat SiOC supported on rGO that has been studied in our group.[16]
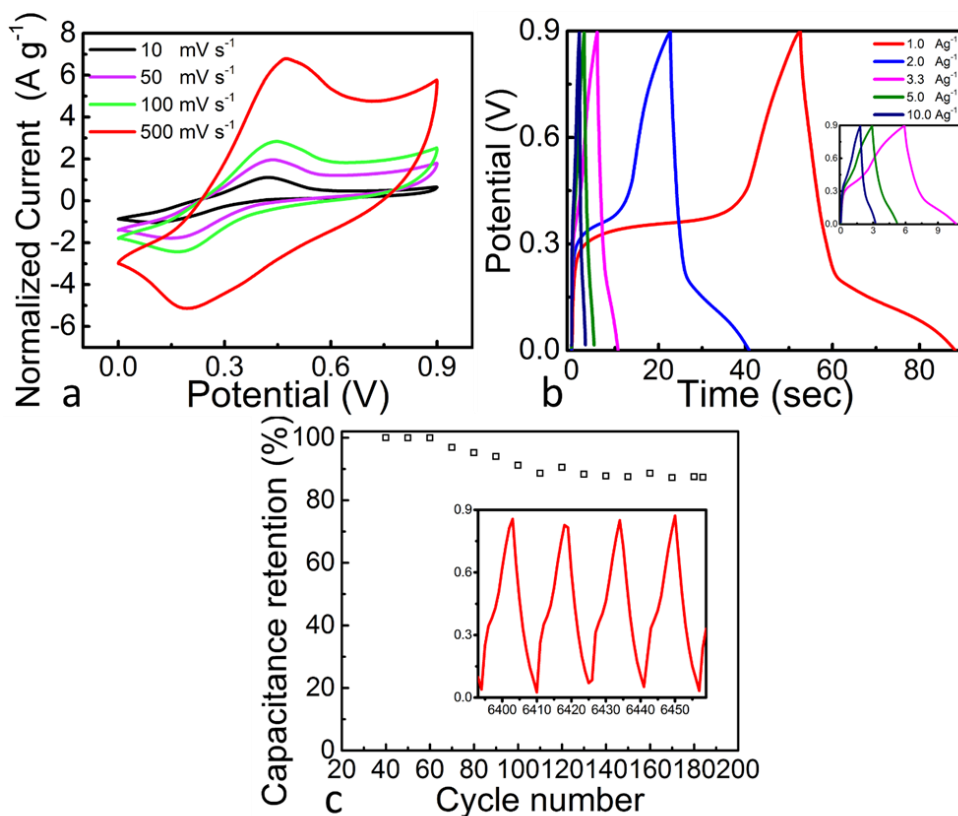
Figure 4-11 (a) Cyclic voltammograms of SiOC-BNNT-0.5 wt.% at different scan rates, (b) Galvanostatic charge-discharge curves at SiOC-BNNT-0.5 wt.% at various current densities, (c) Capacitance retention plot of SiOC-BNNT-0.5 wt.% as a function of cycle number at a current density of density of 1.5 A g^{-1}.

Overall, the application of the SiOC-BNNT composite paper is more promising as a LIB anode material than a supercapacitor. Given the presence of BNNT in the SiOC microstructure, such electrode material can be coupled with devices that can only be powered at high temperature. Also, PDCs are well known for their chemical stability. In light of this, the synthesized SiOC-BNNT composite paper can be used as an electrode material for devices that are routinely used in harsh conditions such as corrosive environments.

4.4 References

1. Xie, S. *et al.* A simply prepared flexible SiBOC ultrafine fiber mat with enhanced high-temperature stability and chemical resistance. *RSC Adv.* **5,** 64911–64917 (2015).

2. Alauzun, J. G. *et al.* Novel monolith-type boron nitride hierarchical foams obtained through integrative chemistry. *J. Mater. Chem.* **21,** 14025 (2011).

3. David, L., Bernard, S., Gervais, C., Miele, P. & Singh, G. Facile synthesis and high rate capability of silicon carbonitride/boron nitride composite with a sheet-like morphology. *J. Phys. Chem. C* **119,** 2783–2791 (2015).

4. Li, J., Bernard, S., Salles, V., Gervais, C. & Miele, P. Preparation of polyborazylene-derived bulk boron nitride with tunable properties by warm-pressing and pressureless pyrolysis. *Chem. Mater.* **22,** 2010–2019 (2010).

5. David, L., Bhandavat, R., Barrera, U. & Singh, G. Silicon oxycarbide glass-graphene composite paper electrode for long-cycle lithium-ion batteries. *Nat. Commun.* **7,** 10998 (2016).

6. Bhandavat, R. & Singh, G. Stable and efficient li-ion battery anodes prepared from polymer-derived silicon oxycarbide-carbon nanotube shell/core composites. *J. Phys. Chem. C* **117,** 11899–11905 (2013).

7. Hong, J., Cho, K.-Y., Shin, D.-G., Kim, J.-I. & Riu, D.-H. Room temperature reaction of polycarbosilane with iodine under different atmospheres for polymer-derived silicon carbide fibres. *RSC Adv.* **5,** 83847–83856 (2015).

8. Sudeep, P. M. *et al.* Functionalized boron nitride porous solids. *RSC Adv.* **5,** 93964–93968 (2015).

9. Tolosa, A. *et al.* Electrospinning and electrospraying of silicon oxycarbide-derived nanoporous carbon for supercapacitor electrodes. *J. Power Sources* **313,** 178–188 (2016).

10. Tuinstra, F. & Koenig, L. Raman Spectrum of Graphite. *J. Chem. Phys.* **53,** 1126–1130 (1970).

11. Peña-Alonso, R., Mariotto, G., Gervais, C., Babonneau, F. & Soraru, G. D. New insights on the high-temperature nanostructure evolution of SiOC and B-doped SiBOC polymer-derived glasses. *Chem. Mater.* **19,** 5694–5705 (2007).

12. Pradeep, V. S., Graczyk-Zajac, M., Riedel, R. & Soraru, G. D. New insights in to the lithium storage mechanism in polymer derived SiOC anode materials. *Electrochim. Acta* **119,** 78–85 (2014).

13. Wilamowska, M., Pradeep, V. S., Graczyk-Zajac, M., Riedel, R. & Sorarù, G. D. Tailoring of SiOC composition as a way to better performing anodes for Li-ion batteries. *Solid State Ionics* **260,** 94–100 (2014).

14. Kroll, P. Tracing Reversible and Irreversible Li Insertion in SiCO Ceramics with Modeling and Ab-Initio Simulations. *MRS Proc.* **1313,** 1–6 (2011).

15. Li, H., Tay, R. Y., Tsang, S. H., Liu, W. & Teo, E. H. T. Reduced Graphene Oxide/Boron Nitride Composite Film as a Novel Binder-Free Anode for Lithium Ion Batteries with Enhanced Performances. *Electrochim. Acta* **166,** 197–205 (2015).

16. Kolathodi, M. S., David, L., Abass, M. A. & Singh, G. Polysiloxane-functionalized graphene oxide paper: pyrolysis and performance as a Li-ion battery and supercapacitor electrode. *RSC Adv.* **6,** 74323–74331 (2016).

17. Graczyk-Zajac, M. *et al.* New Insights into Understanding Irreversible and Reversible

Lithium Storage within SiOC and SiCN Ceramics. *Nanomaterials* **5,** 233–245 (2015).

18. Weng, Q., Wang, X., Wang, X., Bando, Y. & Golberg, D. Functionalized hexagonal boron nitride nanomaterials: emerging properties and applications. *Chem. Soc. Rev.* **45,** 3989–4012 (2016).

19. David, L., Shareef, K. M., Abass, M. A. & Singh, G. Three-dimensional polymer-derived ceramic/graphene paper as a Li-ion battery and supercapacitor electrode. *RSC Adv.* **6,** 53894–53902 (2016).

20. Wu, Z. *et al.* Alternating current line-filter based on electrochemical capacitor utilizing template-patterned graphene. *Sci. Rep.* **5,** 10983 (2015).

21. Hu, H. *et al.* Non-covalent functionalization of graphene with bisphenol a for high-performance supercapacitors. *Chinese J. Chem.* **33,** 199–206 (2015).

22. Kolathodi, M. S., Palei, M. & Natarajan, T. S. Electrospun NiO nanofibers as cathode materials for high performance asymmetric supercapacitors. *J. Mater. Chem. A* **3,** 7513–7522 (2015).

23. Bondavalli, P., Delfaure, C., Legagneux, P. & Pribat, D. Supercapacitor Electrode Based on Mixtures of Graphite and Carbon Nanotubes Deposited Using a Dynamic Air-Brush Deposition Technique. *J. Electrochem. Soc.* **160,** A601–A606 (2013).

24. Sevilla, M. & Fuertes, A. B. Fabrication of porous carbon monoliths with a graphitic framework. *Carbon.* **56,** 155–166 (2013).

Chapter 5 Conclusion and Recommendation

5.1 Conclusion

In summary, the synthesis of a BNNT-modified SiOC ceramic paper via pyrolysis route has been demonstrated. Fabrication of the ceramic composite into a thin film via vacuum filtration provides an inexpensive technique for exploring its application in flexible and lightweight energy storage devices. This thesis explored the feasibility of modifying SiOC by interfacing it preceramic polymer (TTCS) with BNNTs, structural evolution of the modified preceramic polymer to SiOC-BNNT upon pyrolysis at high temperature and potential application as electrode material for LIB and symmetric supercapacitor.

The structural and electrochemical performance of the SiOC-BNNT composite paper was investigated. Structural characterization reveals the absence of significant reaction between the BNNTs and SiOC. As such, the morphology of the BNNTs was preserved after polymer-to-ceramic transformation of the composite. In addition, the presence of disordered carbon known for their electrochemical activity was confirmed in the SiOC-BNNT composite paper, thus the synthesized composite is electrochemically active.

As an anode material for LIB, the SiOC-BNNTs composite containing BNNTs at 0.25 wt.% demonstrated the highest 1st cycle lithiation capacity corresponding to 812 mAh g^{-1}. Charge capacity of the composite decreases with an increase in the BNNT content of the ceramic composite paper. The observed negative trend was attributed to BNNTs (a known insulator which is electrochemically inactive). On the other hand, SiOC interfaced with 0.5 wt.% BNNT demonstrated the highest capacitance (corresponding to 78.93 F g^{-1} a current density of 1.0 A g^{-1}) when tested as an electrode material for symmetric supercapacitor. It is possible that the superior

capacitance of the 0.5 wt.% electrode material is due to the higher ordering of its graphitic planes which is believed to enhance the surface area of the composite since capacitance is dominantly dependent on surface processes.

5.2   Recommendation

In the present configuration, interfacing SiOC with BNNTs results in a lesser charge storage capacity as a battery electrode. With the view of improving the electrochemical performance of the synthesized SiOC-BNNT composite, future work would focus on exploring other routes of introducing BN into the microstructure of SiOC. One approach is to investigate the electrochemical properties of the resulting composite using BN nanosheets in place of BNNTs. The findings from such synthesis route would be pivotal in establishing the effect of BN morphology on the resulting electrochemical performance of the composite.

In addition, the mechanism of charge storage in the BNNT-modified SiOC is yet to be clarified. In later studies, characterization technique such as ^{13}C MAS NMR and ^{29}Si MAS NMR would be used to investigate the chemical states of free carbon and coordinated Si in SiOC.

For the commercialization of the synthesized paper composite, optimization of the composite's porosity, thickness and mechanical properties in addition to its stability to corrosion will be investigated.

Given the presence of BN in the synthesized composite, it is envisaged that synergistic effects between BN and SiOC could result in enhancement of the composite's thermal stability. In this regards, further studies will be focused on characterizing the thermal stability of the composites using techniques that have been reported in the literature.